Article

Decadal-scale droughts disrupted the African Humid Period in the Sahara

https://doi.org/10.1038/s41586-026-10336-7

Received: 18 October 2024

Accepted: 26 February 2026

Published online: 25 March 2026

Check for updates

Florence Sylvestre[1,17]✉, Martin Melles[2,17], Volker Wennrich[2], Michèle Dinies[3], Françoise Chalié[1], Didier Swingedouw[4], Anne Dallmeyer[5], Xiaoxu Shi[6,7], Martin Claussen[5,8], Andrea Jaeschke[2,9], Christine Cocquyt[10,11], Jens Karls[2], Jan Kuper[12], Baba Mallaye[13], Jean-Charles Mazur[1], Christine Paillès[1], Remadji Rirongarti[14], Janet Rethemeyer[2], Benedikt Ritter-Prinz[2], Enno Schefuß[15], Finn Viehberg[2,16], Bernd Wagner[2], Martin Werner[7], Abdallah N. Yacoub[14] & Stefan Kröpelin[12]

During the early and mid-Holocene, the Sahara and Sahel experienced a humid phase, the so-called African Humid Period (AHP)[1]. The AHP started around 14.8 thousand years before present (kyr BP), peaked between 9.0 kyr BP and 6.0 kyr BP and experienced short-lived droughts of as yet poorly constrained age and duration[2,3]. Here we show that the AHP was punctuated by two droughts of decadal-scale duration, at about 9.3 kyr BP and 8.2 kyr BP, and another more tentatively identified drought at 6.3 kyr BP. Our findings arise from a multiproxy time series from the annually layered (varved) sedimentary archive of Lake Yoa in Chad, which covers the past 10.25 kyr continuously. During the more prominent drought at 8.2 kyr BP, pollen and diatom data, along with leaf-wax isotopes and geochemical source area indicators, imply that a reduction in local precipitation and fluvial supply to Lake Yoa caused a lake-level drop accompanied by an expansion of reed belts along the shore. The proxy data, together with our climate simulations, suggest that the 8.2 kyr BP drought event was a direct and rapid response to a potential weakening of the Atlantic Meridional Overturning Circulation (AMOC) owing to sudden freshwater input into the North Atlantic. The results underline the need for improved decadal predictions[4] to better anticipate such drought risks in the future.

In the geological past, the Sahara and Sahel have repeatedly experienced periods with a climate more humid than at present, the so-called AHPs[5]. The most recent AHP occurred between about 14.8 and 5.5 kyr BP (ref. 6) and was strongly time-transgressive, with a later onset and an earlier termination in more northern regions[2,3,7]. During this period, the Sahara was a verdant landscape with vast lakes, such as Megalake Chad[8,9] (Fig. 1b), active drainage systems, the filling up of regional aquifers[10], the thriving of large mammals and flourishing human societies[11].

The AHP was caused by increased summertime insolation, which generated a strong land–sea temperature contrast over North Africa, thus strengthening the African monsoon and carrying rainfall deep into the Sahara[12]. Climate models demonstrate that ocean and land surface feedbacks can alter this initial signal and may result in shifts between wet and dry regimes[13]. Whereas the onset of the last AHP was presumably caused by post-glacial reorganizations of the AMOC, its termination was probably triggered by changes in the meridional gradient of insolation, forced by variations in the precessional cycle of the Earth's orbit[6]. However, climate simulations unequivocally demonstrate that orbital forcing feedbacks in the climate system, mainly those between climate and vegetation, must have played a critical role to explaining the observed changes in the hydrological cycle[14–16].

The last AHP was not a period of constant humid climate. Lake-level records[3,17,18] and reconstruction of western Saharan precipitation derived from leaf-wax isotopes in marine sediments[3] indicate that the last AHP was punctuated by drought events, including a prolonged drought around 8.0 kyr BP. It has been suggested that these droughts are attributed to a weakened AMOC[3]. However, owing to the scarcity of geological records and their insufficient age control, the exact timing of the droughts and their influence on the landscape in the Sahara remains poorly known. This question is relevant not only for palaeoclimate dynamics. Indeed, several climate change projections suggest the risk of a strong and fast slowdown of the AMOC, which could negatively affect West African monsoon rainfall in a few centuries and therefore also the vulnerable populations of the Sahel region[19,20].

[1]Centre de Recherches et d'Enseignement en Géosciences de l'Environnement (CEREGE), Aix-Marseille Université, CNRS, IRD, INRAE, Aix-en-Provence, France. [2]Institute of Geology and Mineralogy, University of Cologne, Cologne, Germany. [3]Institute of Geographical Sciences, Freie Universität Berlin, Berlin, Germany. [4]Environnements et Paléoenvironnements Océaniques et Continentaux (EPOC), Université de Bordeaux, Bordeaux, France. [5]Max Planck Institute for Meteorology, Hamburg, Germany. [6]Southern Marine Science and Engineering Guangdong Laboratory (Zhuhai), Zhuhai, China. [7]Alfred Wegener Institute for Polar and Marine Research, Bremerhaven, Germany. [8]Center for Earth System Research and Sustainability (CEN), Universität Hamburg, Hamburg, Germany. [9]Institute for Crop Science and Resource Conservation (INRES), University of Bonn, Bonn, Germany. [10]Meise Botanic Garden, Meise, Belgium. [11]Limnology Unit, Ghent University, Ghent, Belgium. [12]Institute for Prehistoric Archaeology, University of Cologne, Cologne, Germany. [13]Centre National De Recherche Pour le Développement (CNRD), N'Djaména, Chad. [14]Laboratoire Hydro-Géosciences et Réservoir, Université de N'Djamena, N'Djaména, Chad. [15]MARUM – Center for Marine Environmental Sciences, University of Bremen, Bremen, Germany. [16]University of Greifswald, Institute of Geography and Geology, Greifswald, Germany. [17]These authors contributed equally: Florence Sylvestre, Martin Melles. ✉e-mail: sylvestre@cerege.fr

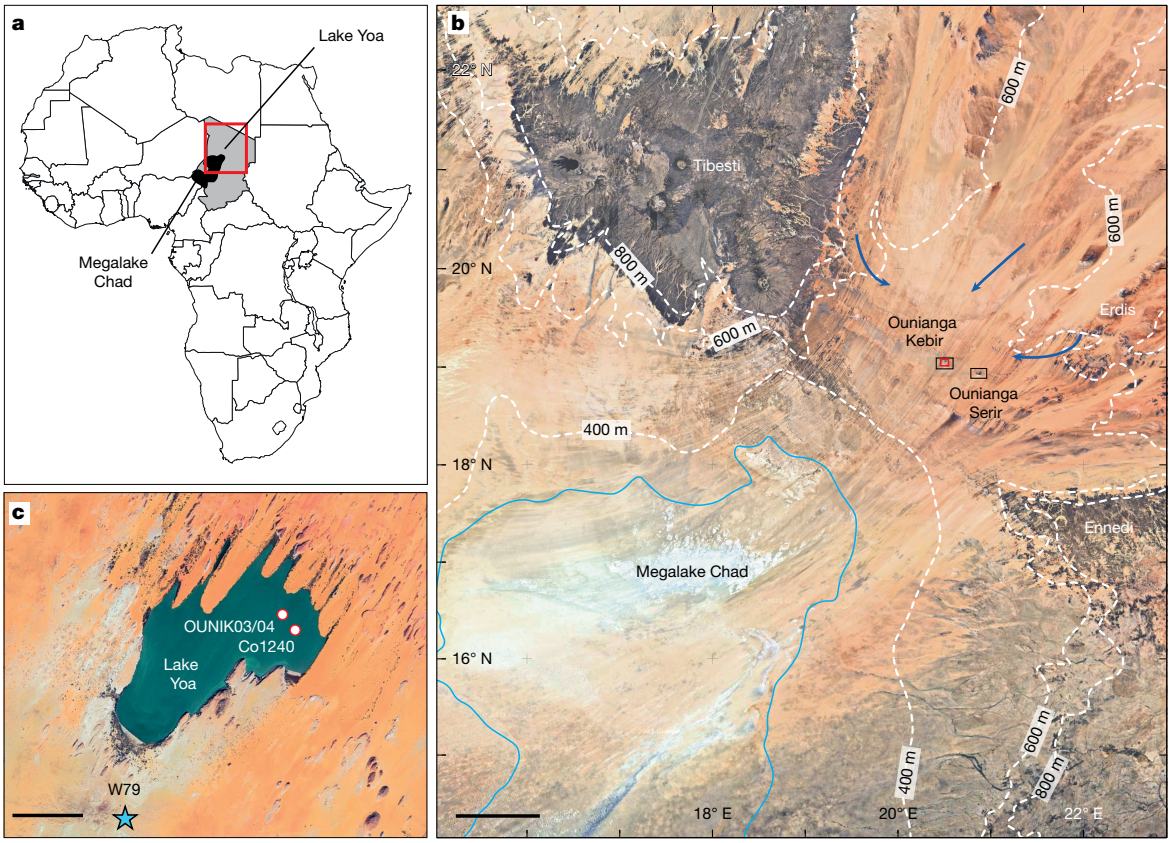

Fig. 1 | Lake Yoa in the context of the central Sahara today and during the early Holocene. a, Geopolitical map of Africa showing the territory of Chad shaded in grey and the locations of Megalake Chad and Lake Yoa (19.03° N, 20.31° E) in the central Sahara. **b**, Satellite image (maps data: Google, 2022, Landsat/Copernicus) of northern Chad (for location, see red frame in **a**) showing the location of Ounianga Kebir and Ounianga Serir between the Ennedi and Tibesti mountains to the north of Megalake Chad (blue line shows the maximum extent during the middle Holocene[9,28]) with altitudes (dashed white lines) and potential water flow from the southeastern Tibesti and the Erdis during moister phases (blue arrows). **c**, Close-up of Lake Yoa, located at 379 m above sea level (for location, see red frame in **b**) showing sand dunes migrating into the lake from the north, the exposure of diatom-rich sediments up to 412 m above sea level (site W79, blue star) and the locations of the coring sites OUNIK03/04 and Co1240 in Lake Yoa (red circles). Maps data: Google, 2024, Maxar Technologies. Scale bars, 100 km (**b**); 1 km (**c**).

The Lake Yoa record

Here we provide the first, to our knowledge, continuous record of hydrological and vegetation changes in the Sahara over the past 10.25 kyr. The record originates from Lake Yoa, which is located at 379 m above sea level in the hyperarid central Sahara at Ounianga Kebir, northern Chad, between the Tibesti and Ennedi mountains (Fig. 1). Lake Yoa today has a maximum depth of 26 m, a surface area of 3.58 km^2 and a catchment area of 67,300 km^2, 28% of which is located in the Tibesti Mountains[21] (Fig. 1b and Extended Data Fig. 1). Despite an extremely negative local water balance, Lake Yoa did not dry out after the AHP owing to persistent groundwater inflow from the wide Nubian Sandstone Aquifer System (NSAS). Previous investigations of the 7.47-m-long lacustrine record OUNIK03/04 (Fig. 1c) have revealed the past 6,000 years of environmental history[22]. The record was extended to the full sedimentary infill of Lake Yoa by the 16.34-m-long composite core Co1240 presented here (Fig. 1c and Extended Data Figs. 2 and 3). According to the age model, sedimentation began around 10.8 kyr BP (Extended Data Fig. 4). The preservation of annual lamination (varves) in 85% of the record allows time control of proxy data to be annual to decadal since about 10.25 kyr BP (Fig. 2a, Methods and Extended Data Figs. 2 and 4–6).

Analyses of sedimentological, geochemical and palaeoecological proxies on the new record highlight the long-term environmental changes in the region, as well as the timing and impact of three short-term droughts that interrupted the AHP (Fig. 2). The endogenic calcite precipitation (Ca and $CaCO_3$ contents; Fig. 2d) reflects evaporative conditions[23]. The Sr/Ca ratio (Fig. 2c) is indicative of sediment supply by surface runoff from the basaltic suites of the Tibesti Mountains, considering their enrichment of Sr (ref. 24). These proxies are combined with indicators of transport energy and sediment supply into the lake (grain size; Fig. 2i), local precipitation (leaf-wax *n*-alkane δD values, pollen-derived humidity index (HI) and phytogeographical regions; Fig. 2f,g and Extended Data Fig. 7), lake-shore vegetation (*Typha* pollen; Fig. 2h and Extended Data Fig. 7) and hydrological and hydrochemical variability (diatoms; Fig. 2b,e and Extended Data Fig. 8).

Long-term environmental changes

Following the formation of Lake Yoa about 10.8 kyr BP, its hydrological and environmental changes took place in four phases (Fig. 2). The phase boundaries were defined by distinct changes in diatom-inferred water conductivity (Fig. 2e). Other proxies responded at slightly different times (Fig. 2), probably because of proxy sensitivity, response time and sampling resolution.

Until about 9.6 kyr BP (phase I), dominant silt and clay with very low sand content (Fig. 2i) indicates that aeolian and fluvial sediment supplies were minor. Relatively light *n*-alkane δD values (Fig. 2f), high pollen-derived HI (Fig. 2g), low percentages of Sudanian and Guinean plant taxa (Extended Data Fig. 7) and very low Sr/Ca ratios (Fig. 2c) suggest that lake formation occurred mainly through infiltration from the NSAS and some local precipitation rather than surface inflow from the Tibesti. Relatively high diatom-inferred conductivities (Fig. 2e) and high calcite

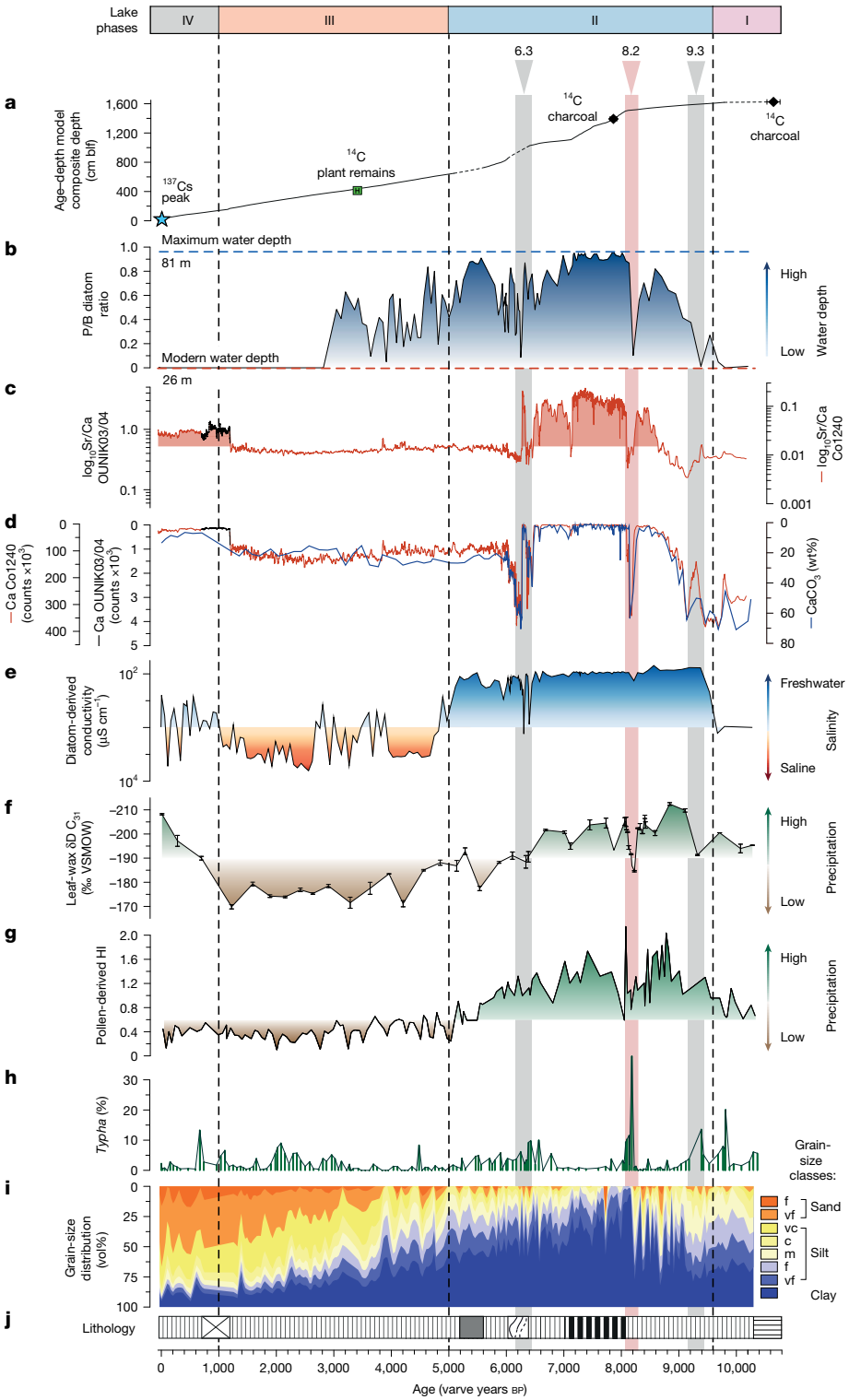

Fig. 2 | Hydrological and environmental changes at Lake Yoa during the past 10.25 kyr. The long-term hydrological changes in Lake Yoa occurred in four phases (I–IV) punctuated by prominent abrupt droughts (marked by grey and red bars). **a**, Age–depth model for the composite core Co1240 as based on triplicate varve counting, confirmed by a ^{137}Cs peak (blue star) and a radiocarbon age of plant remains (green square) in the upper sediments and anchored by a radiocarbon age of grass charcoal (black diamond) in the lower sediments. Another grass charcoal age from the lowermost core catcher indicates the onset of lacustrine sedimentation in Lake Yoa. **b**, Water-depth changes in Lake Yoa reconstructed from the planktonic/benthic (P/B) diatom ratio. Dashed lines indicate the lowest and highest water depths recorded today and during the AHP, respectively. **c**, Sr/Ca ratio ($\log_{10}$) combined for the OUNIK03/04 and Co1240 records. **d**, $CaCO_3$ (%) and Ca (counts) contents combined for the OUNIK03/04 and Co1240 records. **e**, Water conductivity ($\log_{10}$) reconstructed by a diatom-based transfer function. **f**, Compound-specific hydrogen isotope (δD) composition of the most abundant *n*-alkane homologue (*n*-C_{31}) with error bars relative to Vienna Standard Mean Ocean Water (VSMOW). **g**, Pollen-derived humidity index (HI). **h**, Relative abundance of pollen from *Typha* plant taxa. **i**, Grain-size distribution illustrated as a cumulative plot of the clay fraction, five silt fractions and the two finest sand fractions. f, fine; vf, very fine; m, medium; c, coarse; vc, very coarse. **j**, Lithology of the composite core Co1240 (for legend, see Extended Data Fig. 2).

deposition (Fig. 2d) suggest an evaporative water body and the occurrence of *Typha* pollen (Fig. 2h) the presence of reed belts along the shore.

From about 9.6 to 5.0 kyr BP (phase II), Lake Yoa experienced freshwater conditions with very low conductivity (Fig. 2e) and absence of authigenic calcite precipitation (Fig. 2d). Freshwater supply probably originated from increased local rainfall, which is reflected by slightly depleted *n*-alkane δD values until 6.5 kyr BP (Fig. 2f) and may have contributed to the replenishment of the NSAS. Moreover, increased surface inflow from the Tibesti, as indicated by strongly increased Sr/Ca ratios between about 8.6 and 6.2 kyr BP (Fig. 2c) supported a rise in lake level (Fig. 2b). Climate modelling suggests greater than 2,000 mm $year^{-1}$ precipitation at Tibesti around 7.0 kyr BP (ref. 25), which may have led to geomorphic evidence of river channels to the north of Lake Yoa[21] (Fig. 1b and Extended Data Fig. 1).

Other indications of inflow events come from individual, well-sorted clay layers, which were deposited between 8.1 and 7.0 kyr BP (Fig. 2i). The very fine grain size and the lack of any signs of erosion at their bases (Extended Data Fig. 5c,d) exclude formation by sand or dust storms, high-energetic deposition by proximal wave action or proximal river supply, as well as more distal mass-movement events. These characteristics along with high Sr/Ca ratios (Fig. 2c) point to deposition from distal suspension clouds originating from flash floods from the Tibesti. A distal setting of the coring site at that time is also suggested by the maximum water depth of 81 m, 55 m more than today (Methods), which was reached by Lake Yoa during the period of clay layer formation (Fig. 2b). During the water-depth maximum, the lake level has reached 419 m above sea level, thus activating the overflow towards Megalake Chad[21] and implying that Lake Yoa turned from a closed into an open lake system (Extended Data Fig. 1). The lake-level highstand is also reflected by lake sediment sequences with high concentrations of benthic diatoms, which were deposited in only a few metres water depth and crop out at 412 m above sea level in the southern surroundings of Lake Yoa (W79; Fig. 1c). Their formation between 8,054 and 7,956 years BP (ref. 26) coincides with the maximum extents of Megalake Chad and other West and North African lakes[7,27–29].

A gradual change towards today's desert landscape began at 7.0 kyr BP. The reduction in rainfall is reflected by a decrease in the pollen-derived HI (Fig. 2g), lower Sr/Ca ratio (Fig. 2c) and increasing δD values of leaf waxes (Fig. 2f). Simultaneously, the Sudanian vegetation was replaced by Sahelian and later Saharan vegetation (Extended Data Fig. 7). Sediment coarsening with the replacement of clays by medium and coarse silts and later sands (Fig. 2i) reflects an increasing aeolian sediment supply and a lake-level lowering (Fig. 2b), moving the lake shore closer to the coring location.

The lake-level lowering was associated with several fluctuations and a rapid change to saline conditions about 5.0 kyr BP (onset of phase III; Fig. 2b,e), slightly earlier than suggested from the previous OUNIK03/04 record[22]. Between 5.0 and around 1.0 kyr BP, a low HI (Fig. 2g) combined with light δD values of the leaf waxes (Fig. 2f) and low Sr/Ca ratios (Fig. 2c) suggest minima in precipitation. These conditions were associated with a further decreasing lake level (Fig. 2b), combined with carbonate precipitation (Fig. 2d). Particularly dry conditions during phase III are supported by the desiccation of lakes to reed marshes 4.2 kyr BP at Ounianga Serir, east of Lake Yoa[30] (Fig. 1).

After 1.0 kyr BP (phase IV), Sr/Ca ratios (Fig. 2c), carbonate contents (Fig. 2d) and *n*-alkane δD values (Fig. 2f) suggest slightly wetter conditions. This assumption agrees with the development of wetlands and lake-level rises around the same time in Ounianga Serir[30,31] and evidence of flourishing trade and organized kingdoms during much of the eighth to thirteenth centuries CE (ref. 32).

Short-term droughts

The long-term hydrological and environmental changes at Lake Yoa during phase II were interrupted by short-term (<200 years) droughts at approximately 9.3, 8.2 and 6.3 kyr BP (Fig. 2). These events are characterized by lowered humidity levels (Fig. 2g), owing to decreases in rainfall (Fig. 2c,f). This caused lake-level lowerings (Fig. 2b) as well as changes in the lake water ecology (Extended Data Fig. 8) and in catchment vegetation (Fig. 2h and Extended Data Fig. 7). The droughts differ in their effects on the lake-water conductivity (Fig. 2e), the carbonate precipitation (Fig. 2d) and the grain-size distribution (Fig. 2i), as well as in their connection to interregional climate events.

The 9.3 kyr BP drought is reflected by a short-term drop in lake level during the initial period of lake-level rise (Fig. 2b), a decrease in local precipitation (Fig. 2f) and a regression of Sudanian plant taxa (Fig. 2g and Extended Data Fig. 7). Freshwater conditions (Fig. 2e) with limited carbonate precipitation (Fig. 2d) suggest that ion enrichment caused by the evaporation was compensated by fresh groundwater inflow through springs around the lake shore. This drought at Lake Yoa coincides well with drying in the Indian and Asian monsoon domains, as well as cooling at high and middle northern latitudes and is probably linked to meltwater pulses into the North Atlantic from residual ice sheets[33].

The 6.3 kyr BP drought occurred during the transition from high to low lake level (Fig. 2b) as a consequence of decreasing precipitation (Fig. 2c,f). This event shows two excursions in water depth (Fig. 2b), fluvial supply from the Tibesti (Fig. 2c), carbonate precipitation (Fig. 2d) and lake-water salinity (Fig. 2e). These excursions can only be explained by drought; their dichotomy, however, could be an artefact of the deformation in this core interval (Fig. 2j, Extended Data Figs. 2 and 3). A drought at about 6.3 kyr BP has been previously mentioned in several studies, but with poor age control[3,17,18]. This drought is interpreted as a step in the process of aridification, which has led to a notable population collapse in the Sahara region[34]. In Oman, the aridification is traced back to a southward shift of the monsoon rain belt in response to the gradual decrease of insolation[35].

As opposed to the 9.3 and 6.3 kyr BP droughts, the 8.2 kyr BP drought happened during the peak of the AHP, when precipitation was high (Fig. 2c,f) and the lake level reached its maximum (Fig. 2b). The lake-level drop during this event (Fig. 2b) was associated with a sharp increase in carbonate deposition (Fig. 2d) but had little effect on the lake-water conductivity (Fig. 2e), as reflected by high concentrations of freshwater tychoplanktonic diatom species (Extended Data Fig. 8). During this drought, some sites occupied in Niger were temporarily abandoned[36] and fishing and hunting in western Fezzan (Libya) became difficult in the lowlands, driving people to move to neighbouring mountains, where they also began to rely on domesticated animals[37].

The 8.2 kyr BP drought at Lake Yoa coincides with the 8.2 kyr BP climate event[38] (Fig. 3a). This event is clearly related to a reduction of the AMOC in consequence of freshwater supply to the North Atlantic and has led to short-term climate perturbations of nonuniform expression[39,40]. In Greenland, the 8.2 kyr BP event was associated with reductions in temperature and precipitation, the former from 8,212 to 8,141 years BP, with transitions before and after the event comprising 35 years and 55 years, respectively[41]. This is remarkably synchronous with the drought at Lake Yoa, which, according to the floating varve chronology (Fig. 2a), lasted 77 years, from 8,229 to 8,152 years BP, albeit with shorter transitions of 13 years before and 7 years after the event (Extended Data Fig. 6b).

North Atlantic forcings

To assess the potential impact of freshwater inflows into the North Atlantic on precipitation in the central Sahara, we analysed climate model output with respect to the 8.2 kyr event. This event is associated with a constrained forcing and can therefore be explicitly accounted for in climate model simulations.

We first investigated transient Holocene experiments from the TraCE[42] and LOVECLIM[43] models with orbital configurations, greenhouse-gas concentrations, ice-sheet extents and volcanic

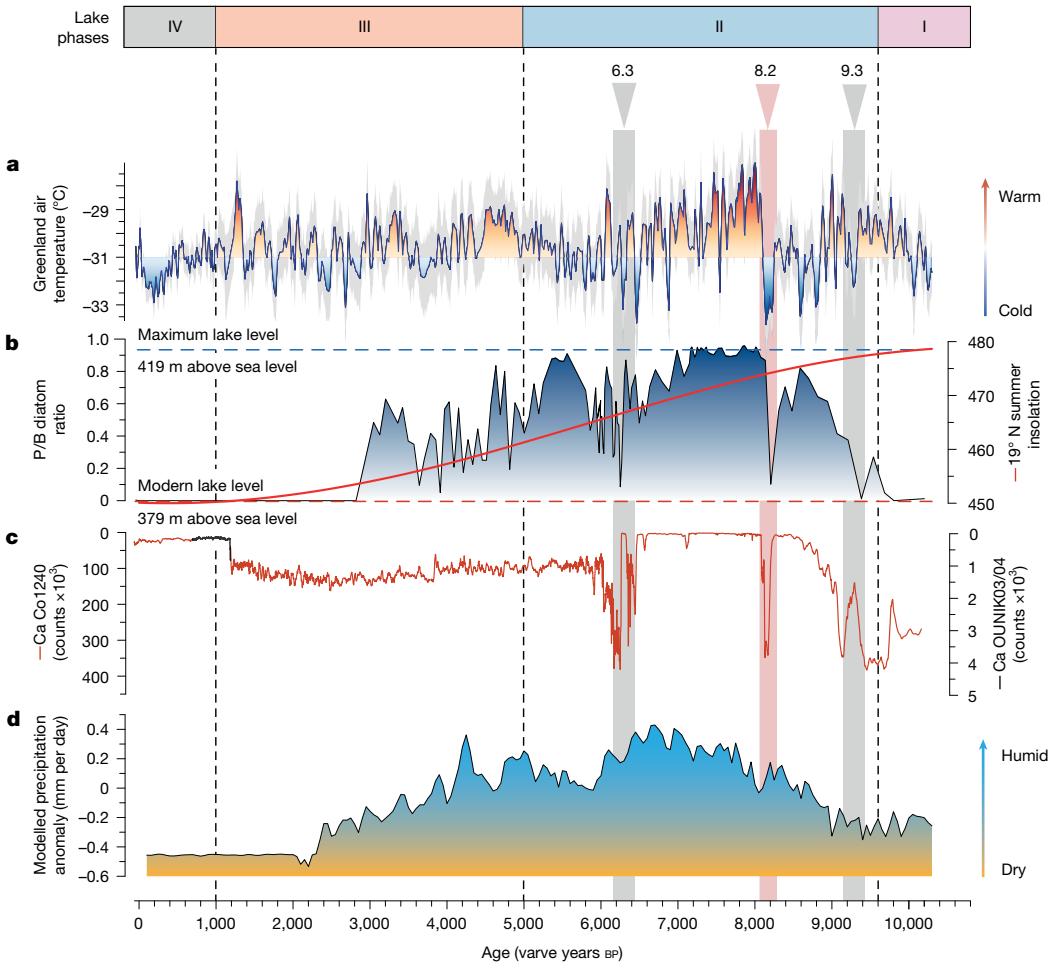

Fig. 3 | The Holocene hydrological history of Lake Yoa compared with North Atlantic climate changes. a–d, Comparison of Greenland temperature reconstruction with 2σ uncertainty from ice cores[38] (**a**) with water-depth changes of Lake Yoa revealed by the P/B diatom ratio and trends in summer insolation at 19° N (red line) (**b**), carbonate precipitation indicated by Ca contents (**c**) and modelled precipitation anomaly (CCSM AMOC-corrected) during the Holocene (**d**) (Extended Data Fig. 9a). The four hydrological phases (I to IV) are indicated and the prominent droughts are marked by grey and red bars.

eruptions (only for LOVECLIM) used as external forcings (Methods). The long-term and short-term precipitation trends obtained (Extended Data Fig. 9) clearly mismatch with the precipitation changes reflected by the Lake Yoa record, showing that the external forcings used fail to explain this precipitation history. Adding an AMOC reconstruction[44] to the transient Holocene experiments (Methods) provided a better match of the long-term trends with the proxy record (Fig. 3 and Extended Data Fig. 9). This suggests that part of the precipitation history at Lake Yoa is related to AMOC changes. The simulations also indicate decadal-scale reductions in precipitation at about 9, 8 and after 6 kyr BP (Fig. 3d). Their temporal deviation from the reconstructed droughts at Lake Yoa may be because of the AMOC reconstruction used here, which is based on stacked marine sea surface temperature records with centennial resolution that is much lower than that provided by the Lake Yoa record (Methods).

Second, we investigated time-slice simulations with the AWI-ESM2-wiso climate model. A prescribed constant freshwater inflow into the Labrador Sea has been set to 0.15 Sv for 100 years, representing a total freshwater amount of 4.67×10^{14} m^3, corresponding to the higher end of the estimates of meltwater release for this event (Methods). We observed that the freshwater inflow reduced precipitation in the Sahel and Sahara regions (Fig. 4) compared with the 8.2 kyr BP control experiment without freshwater forcing in the North Atlantic Ocean (Extended Data Fig. 10). The effect was strongest in West Africa, linked to a weakening of the West African monsoon circulation (Extended Data Fig. 10e), and extended into the central Sahara region in line with our proxy reconstruction from Lake Yoa. In this region, mean annual rainfall decreased by approximately 50–100 mm year^{-1}. The overall reduction in precipitation over the entire Sahara and Sahel region (Fig. 4) would have caused a large-scale decrease also in runoff and groundwater flow and, hence, could have had a large effect on the dynamics and level of Lake Yoa. The sensitivity experiments therefore support our interpretation that past AMOC changes could have driven part of the 8.2 kyr BP drought event observed in our record.

The palaeoenvironmental reconstruction presented here from Lake Yoa, complemented by climate simulations, provides new information on the long-term, millennial-scale hydrological and environmental changes that have occurred in the central Sahara region in the course of the insolation-driven AHP. It also highlights the climate and environmental changes associated with short-term changes in the African monsoon, particularly with the 8.2 kyr BP drought event substantially supported by an AMOC reduction in consequence of freshwater inflow into the North Atlantic Ocean. Today, the AMOC seems to weaken owing to accelerated melting of the Greenland Ice Sheet[45], a trend that will probably continue throughout the twenty-first century[46] and beyond[47]. The boundary conditions between the early Holocene and today are substantially different, for example, in the size of ice sheets, sea level, vegetation cover and insolation, the last of these inducing strong consequences for monsoon dynamics. However, the reconstruction from Lake Yoa highlights how far into the Sahara region AMOC-triggered

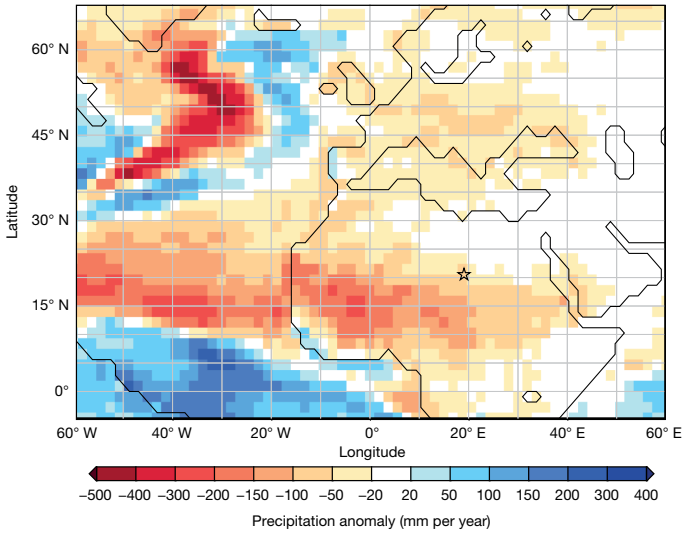

Fig. 4 | Simulated precipitation changes for the 8.2 kyr BP event. Difference in precipitation between the AWI-ESM simulations with constant freshwater input into the Labrador Sea and the simulation without freshwater input. The location of Lake Yoa is marked by a star.

droughts can reach, how quick the associated precipitation changes can occur and what consequences these can have on regional ecosystems. The results indicate that such changes could have severe consequences for the vulnerable Sahara region at the decadal scale, with a substantial decrease in the cultivatable area that can lead to strong human migration pressure.

Online content

Any methods, additional references, Nature Portfolio reporting summaries, source data, extended data, supplementary information, acknowledgements, peer review information; details of author contributions and competing interests; and statements of data and code availability are available at https://doi.org/10.1038/s41586-026-10336-7.

1. deMenocal, P. et al. Abrupt onset and termination of the African Humid Period: rapid climate responses to gradual insolation forcing. *Quat. Sci. Rev.* **19**, 347–361 (2000).
2. Gasse, F. Hydrological changes in the African tropics since the Last Glacial Maximum. *Quat. Sci. Rev.* **19**, 189–211 (2000).
3. Tierney, J. E., Pausata, F. S. R. & deMenocal, P. B. Rainfall regimes of the Green Sahara. *Sci. Adv.* **3**, e1601503 (2017).
4. Swingedouw, D. et al. Early warning from space for a few key tipping points in physical, biological, and social-ecological systems. *Surv. Geophys.* **41**, 1237–1284 (2020).
5. Crocker, A. J. et al. Astronomically controlled aridity in the Sahara since at least 11 million years ago. *Nat. Geosci.* **15**, 671–676 (2022).
6. Shanahan, T. M. et al. The time-transgressive termination of the African Humid Period. *Nat. Geosci.* **8**, 140–144 (2015).
7. Lézine, A.-M., Hély, C., Grenier, C., Braconnot, P. & Krinner, G. Sahara and Sahel vulnerability to climate changes, lessons from Holocene hydrological data. *Quat. Sci. Rev.* **30**, 3001–3012 (2011).
8. Quade, J. et al. Megalakes in the Sahara? A review. *Quat. Res.* **90**, 253–275 (2018).
9. Ghienne, J.-F., Schuster, M., Bernard, A., Duringer, P. & Brunet, M. The Holocene giant Lake Chad revealed by digital elevation models. *Quat. Int.* **87**, 81–85 (2002).
10. Mohamed, A., Ahmed, E., Alshehri, F. & Abdelrady, A. The groundwater flow behavior and the recharge in the Nubian Sandstone Aquifer System during the wet and arid periods. *Sustainability* **14**, 6823 (2022).
11. Kuper, R. & Kröpelin, S. Climate-controlled Holocene occupation in the Sahara: motor of Africa's evolution. *Science* **313**, 803–807 (2006).
12. Kutzbach, J. E. & Otto-Bliesner, B. The sensitivity of the African-Asian monsoonal climate to orbital parameter changes for 9000 years B.P. in a low-resolution general circulation model. *J. Atmos. Sci.* **39**, 1177–1188 (1982).
13. Brovkin, V., Claussen, M., Petoukhov, V. & Ganopolski, A. On the stability of the atmosphere-vegetation system in the Sahara/Sahel region. *J. Geophys. Res. Atmos.* **103**, 31613–31624 (1998).
14. Claussen, M. & Gayler, V. The greening of the Sahara during the mid-Holocene: results of an interactive atmosphere-biome model. *Glob. Ecol. Biogeogr. Lett.* **6**, 369–377 (1997).
15. Braconnot, P., Joussaume, S., Marti, O. & de Noblet, N. Synergistic feedbacks from ocean and vegetation on the African monsoon response to mid-Holocene insolation. *Geophys. Res. Lett.* **26**, 2481–2484 (1999).
16. Braconnot, P. et al. Results of PMIP2 coupled simulations of the Mid-Holocene and Last Glacial Maximum – part 2: feedbacks with emphasis on the location of the ITCZ and mid- and high latitudes heat budget. *Clim. Past* **3**, 279–296 (2007).
17. Gasse, F. & Van Campo, E. Abrupt post-glacial climate events in West Asia and North Africa monsoon domains. *Earth Planet. Sci. Lett.* **126**, 435–456 (1994).
18. Servant, M. & Servant-Vildary S. in *The Sahara and the Nile* (eds Williams, M. A. J. & Faure, H.) 133–162 (Balkema, 1980).
19. Defrance, D. et al. Consequences of rapid ice sheet melting on the Sahelian population vulnerability. *Proc. Natl Acad. Sci. USA* **114**, 6533–6538 (2017).
20. Ben-Yami, M. et al. Impacts of AMOC collapse on monsoon rainfall: a multi-model comparison. *Earths Future* **12**, e2023EF003959 (2024).
21. Grenier, C., Paillou, P. & Maugis, P. Assessment of Holocene surface hydrological connections for the Ounianga lake catchment zone (Chad). *C. R. Geosci.* **341**, 770–782 (2009).
22. Kröpelin, S. et al. Climate-driven ecosystem succession in the Sahara: the past 6000 years. *Science* **320**, 765–768 (2008).
23. Francus, P. et al. Varved sediments of Lake Yoa (Ounianga Kebir, Chad) reveal progressive drying of the Sahara during the last 6100 years. *Sedimentology* **60**, 911–934 (2013).
24. Gourgaud, A. & Vincent, P. M. Petrology of two continental alkalineintraplate series at Emi Koussi volcano, Tibesti, Chad. *J. Volcanol. Geotherm. Res.* **129**, 261–290 (2004).
25. Hoelzmann, P. et al. Mid-Holocene extreme precipitation in the Tibesti, Central Sahara. *Nat. Commun.* **16**, 7426 (2025).
26. Sylvestre, F. et al. Decadal-scale droughts disrupted the African Humid Period in the Sahara. *Zenodo* https://doi.org/10.5281/zenodo.13912623 (2026).
27. Hoelzmann, P. et al. Mid-Holocene land-surface conditions in northern Africa and the Arabian Peninsula: a data set for the analysis of biogeophysical feedbacks in the climate system. *Global Biogeochem. Cycles* **12**, 35–51 (1998).
28. Schuster, M. et al. Holocene Lake Mega-Chad palaeoshorelines from space. *Quat. Sci. Rev.* **24**, 1821–1827 (2005).
29. Sylvestre, F. et al. in *Le Tchad des Lacs. Les Zones Humides Sahéliennes au Défi du Changement Global* (eds Raimond, C., Sylvestre, F., Zakinet, D. & Abderamane, M.) 53–64 (IRD, 2019).
30. Van der Meeren, T. et al. A predominantly tropical influence on late Holocene hydroclimate variation in the hyperarid central Sahara. *Sci. Adv.* **8**, eabk1261 (2022).
31. Creutz, M., Van Bocxlaer, B., Abderamane, M. & Verschuren, D. Recent environmental history of the desert oasis lakes at Ounianga Serir, Chad. *J. Paleolimnol.* **55**, 167–183 (2016).
32. Maley, J. & Verney, R. Populations and climatic evolution in north tropical Africa from the end of the Neolithic to the dawn of the modern era. *Afr. Archaeol. Rev.* **32**, 179–232 (2015).
33. Fleitmann, D. et al. Evidence for a widespread climatic anomaly at around 9.2 ka before present. *Paleoceanography* **23**, PA1102 (2008).
34. Manning, K. & Timpson, A. The demographic response to Holocene climate change in the Sahara. *Quat. Sci. Rev.* **101**, 28–35 (2014).
35. Fleitmann, D. et al. Holocene ITCZ and Indian monsoon dynamics recorded in stalagmites from Oman and Yemen (Socotra). *Quat. Sci. Rev.* **26**, 170–188 (2007).
36. Sereno, P. C. et al. Lakeside cemeteries in the Sahara: 5000 years of Holocene population and environmental change. *PLoS One* **3**, e2995 (2008).
37. Cremaschi, M. et al. Takarkori rock shelter (SW Libya): an archive of Holocene climate and environmental changes in the central Sahara. *Quat. Sci. Rev.* **101**, 36–60 (2014).
38. Kobashi, T. et al. Volcanic influence on centennial to millennial Holocene Greenland temperature change. *Sci. Rep.* **7**, 1441 (2017).
39. Rohling, E. J. & Pälike, H. Centennial-scale climate cooling with a sudden cold event around 8,200 years ago. *Nature* **434**, 975–979 (2005).
40. Parker, S. E. & Harrison, S. P. The timing, duration and magnitude of the 8.2 ka event in global speleothem records. *Sci. Rep.* **12**, 10542 (2022).
41. Thomas, E. R. et al. The 8.2 ka event from Greenland ice cores. *Quat. Sci. Rev.* **26**, 70–81 (2007).
42. Liu, Z. et al. Transient simulation of last deglaciation with a new mechanism for Bolling–Allerod warming. *Science* **325**, 310–314 (2009).
43. Goosse, H. et al. Description of the Earth system model of intermediate complexity LOVECLIM version 1.2. *Geosci. Model. Dev.* **3**, 603–633 (2010).
44. Ayache, M., Swingedouw, D., Mary, Y., Eynaud, F. & Colin, C. Multi-centennial variability of the AMOC over the Holocene: a new reconstruction based on multiple proxy-derived SST records. *Glob. Planet. Change* **170**, 173–183 (2018).
45. Caesar, L., McCarthy, G. D. & Rahmstorf, S. Current Atlantic Meridional Overturning Circulation weakest in last millennium. *Nat. Geosci.* **14**, 118–120 (2021).
46. Intergovernmental Panel on Climate Change (IPCC). *Climate Change 2021: The Physical Science Basis. Contribution of Working Group I to the Sixth Assessment Report of the Intergovernmental Panel on Climate Change* (eds Masson-Delmotte, V. et al.) (Cambridge Univ. Press, 2021).
47. Drijfhout, S., Angevaare, J. R., Mecking, J., van Westen, R. M. & Rahmstorf, S. Shutdown of northern Atlantic overturning after 2100 following deep mixing collapse in CMIP6 projections. *Environ. Res. Lett.* **20**, 094062 (2025).

Methods

Lakes and regional hydrology

Lake Yoa (19° 03′ N, 20° 31′ E, 379 m above sea level) is located in the central Sahara in northern Chad (Fig. 1). The lake is part of the Ounianga Lakes district, the largest permanent aquatic ecosystem of the Sahara. This district comprises Ounianga Kebir to the west and Ounianga Serir to the east (Fig. 1 and Extended Data Fig. 1). These areas have been classified since 2012 as a natural World Heritage Site by the United Nations Educational, Scientific and Cultural Organization (UNESCO) in recognition of the unique natural occurrence of several permanent lakes.

The Ounianga Lakes spread in Pleistocene deflation basins at the foot of an east–west-oriented escarpment of the Mesozoic Nubian Sandstone Complex[48,49]. The valley network indicates water inflow from the northwest (Tibesti) and east (Erdis) (Extended Data Fig. 1). To the south, the lakes are bordered to the Lake Chad basin by an overflow divide at approximately 419 m above sea level[21]. Today, the Ounianga Lakes are almost exclusively fed by fossil fresh groundwater from the NSAS[48,50,51]. Radiocarbon dating indicates that the groundwater has an age of roughly 10,000 calendar years BP (ref. 52), placing it within the onset of the AHP[6].

The Ounianga Lakes district is characterized by a subtropical desert climate resulting from its continental and low-latitude position combined with the present-day location of the Intertropical Convergence Zone[53]. The region experiences only erratic rainfall of <20 mm year^{-1} and extreme evaporation of >6,000 mm year^{-1} (refs. 54,55). It is exposed to strong near-surface winds predominantly from the northeast and mainly during the winter months[56]. The monthly average temperatures vary from 14 °C to 30 °C (ref. 55). The vegetation surrounding the lake is of the Saharan type[57], predominantly fed by groundwater discharge from springs.

Lake Yoa represents the largest lake in Ounianga Kebir. Today, it has a surface area of 3.58 km^2 and a maximum water depth of about 26 m. The lake is not connected to any active hydrographical network[21,54] but is essentially fed by springs with conductivities ranging from 100 µS cm^{-1} to 250 µS cm^{-1} (refs. 52,58). Monitoring carried out between November 2010 and February 2012 shows that the lake experienced complete mixing from October to January and stratification culminated between July and September[59]. From the surface to the bottom, the water column showed a pH of about 10, an increase in conductivity from 66,200 µS cm^{-1} to 68,000 µS cm^{-1}, a decrease in temperature from 21 °C to 16 °C and a decrease in oxygen saturation from 45% to 5%. Owing to the almost exclusive groundwater supply, the seasonal lake-level variations do not exceed 1.0 m (ref. 55). The water residence time amounts to approximately 3.4 years (ref. 51).

Coring and development of the composite core

Coring site Co1240 (19° 03.456′ N, 20° 30.915′ E) is located in the northeastern part of Lake Yoa, about 500 m away from the southern shore and about 600 m from the northern shore, at which dunes prograde into the lake (Fig. 1c). Coring was carried out in 2010 from a floating platform (UWITEC Corp.). A gravity corer was used to recover the uppermost lake sediments down to 1.12 m below the lake floor (blf) (Extended Data Fig. 2). Deeper sediments from overlapping sections were recovered with a 3-m-long percussion piston corer. On the basis of matching lithologies and Ti counts (2-mm resolution, see below), overlapping core segments from two gravity cores and nine piston cores were spliced into a 16.34-m-long composite sediment record (Extended Data Fig. 2). A gap was identified between 1.12 and 1.64 m blf and bridged with data from the core succession OUNIK03/04, which was recovered approximately 150 m to the northwest of coring site Co1240 (refs. 22,23) (Fig. 1c).

Core lithology

The composite core Co1240 starts with crudely stratified, poorly sorted sediments that contain weathered sandstone fragments at its base, which prevented further penetration of the piston corer (Extended Data Fig. 2). Together with hydroacoustic data, these findings suggest that the whole lake-sediment infilling was recovered. Above 16.19 m blf, the core consists of fine-grained laminated sediments of clastic, biogenic and authigenic origin. Francus et al.[23] investigated the laminations in the 7.47-m-long core succession OUNIK03/04 and confirmed their annual formation (varves). Our Co1240 core contains similar laminations (Extended Data Figs. 5 and 6) complemented by irregularly intercalated clay layers of up to 20 mm thickness in the interval between 15.05 and 9.50 m blf (Extended Data Figs. 2, 3 and 5). The clay layers contain <40% silt and no coarser grains, which is too fine-grained for an aeolian formation by dust or sand storms[60] or near-shore, wave-dominated deposition. Their massive appearance and sharp but non-erosive lower boundaries (Extended Data Fig. 2) further exclude a formation by mass-movement events, such as turbidity currents. Hence, it is most likely that the clay layers were deposited from very-fine-grained suspension in a deep stagnant water body, with the suspension being the distal overflow component of fluvial sediment supply. The water depth at that time can have reached 81 m blf, 55 m more than today, taking in account the overflow altitude (419 m above sea level), the modern lake level (379 m above sea level), the current water depth (26 m) and the thickness of the sediments above the clay layers (15 m).

Chronology

The chronology of the composite core Co1240 (Fig. 2a and Extended Data Fig. 4) is based on varve counting, supported by a ^{137}Cs peak in the uppermost sediments and ^{14}C ages of grass charcoal and plant remains in the deeper sediments.

Varve counting was conducted on linescan colour images of the split-core sediment surfaces, complemented by X-radiographs, high-resolution X-ray fluorescence (XRF) data and thin sections for transmitted light microscopy (for examples, see Extended Data Fig. 5). A full documentation of the varve counts is provided in the Zenodo repository[26]. Starting from the top, the number of varves throughout 10-cm-thick increments was recorded. Counting was carried out three times by two different analysts and the mean values were used to construct the age-depth model and to calculate the sedimentation rates. The duration of the gap in the upper part of core Co1240 (1.12–1.64 m blf) was derived from the chronology of the respective sediments in core OUNIK03/04 (ref. 22) and a correlation of both cores based on Ti counts[23] (Extended Data Fig. 2). Varve counting was also not possible in the intervals 6.50–7.28 m and 8.48–10.04 m blf, in which lamination is deformed and the sediment is partly homogenized (Extended Data Figs. 2 and 3). The age–depth models for these core parts are based on extrapolation of the sedimentation rates in the varved sediments 10 cm below and above the partly disturbed sediments. The average error derived from the triplicate counting is ±8 years, with up to 53 years in intervals with low sedimentation rate or faint lamination.

A ^{137}Cs peak 7 cm below the sediment surface in the OUNIK03/04 record[22] is ascribed to the nuclear-bomb-testing peak AD 1963 (ref. 61). This peak transfers to 14 cm depth in the gravity core Co1240-1 based on the correlation of comparable lamination patterns in both cores, in which the varve counts suggest exactly the same age of AD 1963 (ref. 26) (Extended Data Fig. 6a). This confirms undisturbed sampling of the sediment surface[22] and that the laminations in the upper part of the record represent annual deposition[23].

^{14}C dating was performed on both cores, using bulk carbonate (n = 2), bulk organic matter (n = 35), *Typha* rhizome (n = 5), undefined plant material (n = 1) and grass charcoal (n = 4), following the standard acid–alkali–acid extraction protocol[62]. Furthermore, compound-specific ^{14}C dating of long-chain n-fatty acids (C_{24} and/or C_{28}) was performed on bulk sediment (n = 4) following extraction and separation after ref. 63. ^{14}C samples were measured at Beta Analytic Limited, Miami (USA), the CologneAMS facility (Germany), the AMS facility of the Swiss

Federal Institute of Technology (ETH) Zurich (Switzerland), the Poznań Radiocarbon Laboratory (Poland) and the Rijksuniversiteit Groningen Radiocarbon Laboratory (The Netherlands). The radiocarbon dates were calibrated using the OxCal 4.4 software package[64] with the IntCal 2020 calibration dataset[65].

The calendar ages derived by ^{14}C dating of plant remains and grass charcoal[26] are very similar to those obtained by varve counting[26] (Extended Data Fig. 4). This suggests that they are unaffected by reservoir effects, as found in other lake sediment records previously[22,66]. Hence, the match of the ^{14}C age of the plant remains from 4.13 m blf (3,421 ± 27 calendar years BP) with the varve age (3,214 ± 6 varve years BP) confirms annual lamination down to 6.50 m blf in the part of the record that is anchored by the sediment surface and the ^{137}Cs peak (see above). Moreover, the good agreement of the grass-charcoal ^{14}C age from 13.92 m blf (7,883 ± 58 calendar years BP) with the respective varve age (7,868 ± 6 varve years BP) supports the extrapolation of the varve counts over the intervals 6.50–7.28 m and 8.48–10.04 m blf and thus the floating varve chronology. The lowermost grass-charcoal ^{14}C age from the core catcher (16.31 m blf; 10,672 ± 114 calendar years BP) is used to date the sediments below the basal varve age (16.19 m blf; 9,814 ± 36 varve years BP) by linear extrapolation to the ^{14}C age and is important for the timing of the onset of lake sedimentation.

In contrast to the ^{14}C ages of plant remains and grass charcoal, the ^{14}C ages of plant wax *n*-fatty acids slightly overestimate the varve ages, possibly because of some delay between the fatty acid formation and deposition. A stronger bias by reservoir effects is reflected by the ^{14}C ages of bulk organic matter and *Typha* rhizomes in Lake Yoa, as already found in ref. 22. The same holds true for a bulk carbonate ^{14}C age from 8.91 m blf (sample Beta-293232), whereas a second bulk carbonate age (sample Beta-293233) is unrealistically young and thus was considered an outlier. The reservoir effect is reflected by the differences between the varve counts and the uncorrected ^{14}C ages of bulk organic matter, *Typha* rhizomes and bulk carbonate (Extended Data Fig. 4); it is constant at approximately 1,500 years in the upper part of the record, whereas it decreases between about 10 and 12 m blf to values <500 years.

As a result, the age–depth model strongly suggests that lacustrine sedimentation in Lake Yoa began at around 10,800 years BP and has continued until the present (Extended Data Fig. 4). The sedimentation rates were the lowest (average 0.5 mm year^{-1}) in the early stage of the lake history, strongly increased in value and variability between about 8,200 and 5,600 calendar years BP (average 3.9 mm year^{-1}; varying from 0.7 to 9.1 mm year^{-1}) and became relatively constant (average 1.3 mm year^{-1}) since then.

Complementary ^{14}C dating was carried out on carbonates from lake sediments exposed to the south of Lake Yoa[26] (site W79, Fig. 1c) to estimate the altitude and timing of the maximal lake-level highstand. The carbonate radiocarbon ages were first transformed into bulk organic matter ages, taking the age difference of 380 years between carbonate and bulk organic matter at 8.91 m blf depth of the composite core. The bulk organic matter ages were then calibrated into calendar ages using the OxCal 4.4 software package[64] with the IntCal 2020 calibration dataset[65] and subsequently transferred into varve ages by subtracting the age difference between the Bayesian and the varve age models at the corresponding depths in the composite core during the Bayesian times of deposition (Extended Data Fig. 4).

Grain-size and geochemical analyses

For grain-size analyses of the lithogenic material, approximately 1.0-g aliquots were treated with hydrogen peroxide (H_2O_2, 35%), HCl (10%) and sodium hydroxide (NaOH, 1 M) to remove the organic material, calcium carbonate and biogenic silica, respectively. Subsequently, the aliquots were dispersed on a shaker for 12 h after adding 60 ml of deionized water with sodium pyrophosphate ($Na_4P_2O_7$, 2.5 g l^{-1}) and 1 min of ultrasonic treatment. Grain-size analyses were performed using a Saturn DigiSizer 5200 laser-particle analyser (Micromeritics Co.). Grain-size statistics were calculated with the software GRADISTAT version 8.0 (ref. 67) and are given according to the method in ref. 68.

Variations in inorganic geochemistry were determined using non-destructive XRF scanning on half-cores. Before the measurement, the sediment surface was carefully levelled and covered with an Ultra-Polyester Thin Film (1.5 µm) (Chemplex). Scanning was performed at 2-mm intervals using an ITRAX core scanner (Cox Analytical Systems)[69] equipped with a 1.9-kV chromium (Cr) X-ray source and a Si-drift detector in combination with a multichannel analyser. Voltage, amperage and exposure time were set to 30 kV, 30 mA and 20 s, respectively. Spectral evaluation and data processing were performed using the software QSpec 6.5 (Cox Analytical Systems).

For analyses of total inorganic carbon (TIC), an aliquot of 0.5 g of each sample was homogenized and ground to <63 µm in a planetary mill. TIC was measured with a DIMATOC 100 carbon analyser (Dimatec Analysentechnik GmbH) on CO_2 released through the reaction with orthophosphoric acid (H_3PO_4; 40%) at 160 °C. The $CaCO_3$ concentrations were calculated from the TIC contents and the atomic weights of the elements in calcite.

Compound-specific hydrogen isotope (δD) analysis of the most abundant *n*-alkane homologues (*n*-C_{29} and *n*-C_{31}) was performed on a Thermo Scientific TRACE GC coupled by means of a combustion reactor to a Thermo Fisher MAT 253 mass spectrometer. The GC was equipped with a 30 m × 0.25 mm column (Restek Rxi-5ms, film thickness 1.0 µm) and He was used as the carrier gas. The fractions were injected using a PTV injector at 40 °C and then transferred to the GC column. The GC temperature was programmed to increase from 120 °C (2 min hold) to 200 °C at a rate of 30 °C min^{-1} and then at 4 °C min^{-1} to 320 °C (held for 12.3 min). H_2 was used as a reference gas; δD values are given in ‰ relative to Vienna Standard Mean Ocean Water (VSMOW). The H3 factor monitored on a daily basis had a mean of 6.00 ± 0.02. An external standard mixture with known δD values was analysed repeatedly every six runs, yielding a long-term mean standard deviation of <3‰ and a mean deviation of <1‰ from the reference values. All samples were analysed in duplicate with an average standard deviation of 2‰.

Palynology processing and data analysis

Published palynological data from Lake Yoa, which were obtained from core OUNIK03/04 (Fig. 1c) and cover the past 5.2 kyr BP (refs. 22,57), were complemented by palynological analyses of 76 samples collected from the lower part of core Co1240 deposited between 10.4 and 5.2 kyr BP. These samples of 1–5 cm^3 (ref. 26) were treated with HCl (10% at 95 °C) and potassium hydroxide (KOH 10%) to dissolve carbonates and humic acids, respectively. Sample preparation differed to that used for OUNIK03/04 by density separation using sodium polytungstate (SPT; $Na_6H_2W_{12}O_{40}$, ρ = 2.01 g cm^{-3}) instead of hydrofluoric acid treatment to remove the minerogenic fraction[70,71]. The SPT method has been shown to provide results comparable with the hydrofluoric acid treatment[72]. Duplicate analyses of Co1240 samples from the interval <5.2 kyr BP treated with SPT yield results comparable with the respective OUNIK03/04 counts[26], thus confirming no marked biases between the two preparation methods. Subsequent acetolysis (acetic anhydride and sulfuric acid; ratio 9:1) and sieving (< 5 µm) were conducted to reduce organic components, such as (hemi)cellulose and fine-grained particles[72]. The pollen concentrates were mounted with glycerine and counted under a Leica DM2000 microscope at 400× magnification. Pollen sample residues are stored at the Institute of Geographical Sciences of Freie Universität Berlin.

Pollen and selected non-pollen palynomorphs (fern spores, fungal remains, algae other than diatoms and charred plant particles) were identified using published atlases[73–80] and online databases[81–86], as well as the reference collection of Freie Universität Berlin. The identified pollen types were harmonized with those determined by Kröpelin et al.[22] and Lézine et al.[57] to assure data comparability within the core

composite, resulting in a total of 185 different pollen types. A mean sum of 411 (32-1381, four samples <150) terrestrial pollen grains and fern spores were counted and assigned to pollen types. Pollen percentages were calculated to the sum of terrestrial types, with exclusively aquatic and palustrine pollen types (for example, *Typha* and Cyperaceae) as well as non-pollen palynomorphs being excluded.

For vegetation reconstructions for the past 10.4 kyr BP, the full pollen dataset from cores OUNIK03/04 and Co1240 was used, excluding rare pollen types with occurrences ≤1% (ref. 87) observed in fewer than ten samples. Following previous palynological studies of Northern Africa[88–90], pollen types were assigned to the Saharan, Sahelian, Sudanian, Guinean and mountainous phytogeographical regions[26] (Extended Data Fig. 7b). From north to south, the large Saharan desert region passes into the Sahelian phytoregion, which is characterized by unreliable rainfall of 150–500 mm, mainly in summer, and a pronounced and long dry season. To the south of about 15° N, the Sudanian region, which belongs to the tropical summer-rainfall zone with a dry season of 5–7 months, passes into the Guinean equatorial region, which is characterized by a humid monsoonal climate. Thereby, pollen types are often assigned to several phytoregions. *Tribulus*, for example, is assigned 50% to the Saharan and 50% to the Sahelian regions. Pollen types that have only been identified at the family level were excluded. For visualization of the summed Guinean, Sudanian, Sahelian and Saharan proportions, the *z*-scores were calculated (Extended Data Fig. 7b). Shifts in the proportions of the assigned phytoregions over time are assumed to indicate changes in humidity and seasonality.

The pollen-derived HI (Fig. 2g and Extended Data Fig. 7a) is based on the phytogeographical affinity of each sample. Therefore, the square root (sqrt) and centre log ratio (clr) transformed counts of a pollen type were multiplied by its respective phytogeographical indication. Samples with fewer than three phytogeographically assigned pollen types and/or fewer than nine assigned pollen type counts were excluded. The HI of a sample has been calculated from the ratio between the proportions of more humid (Guinean, Sudanian) to more arid phytoregions (Sudanian, Sahelian, Saharan) as follows:

$$\mathrm{HI} = (\mathrm{Grasses(sqr,\ clr)} \times \mathrm{Guinean(sqrt,\ clr)} + \mathrm{Sudanian(sqrt,\ clr)})/(0.5 \times \mathrm{Sudanian(sqrt,\ clr)} + \mathrm{Sahelian(sqrt,\ clr)} + \mathrm{Saharan(sqrt,\ clr)})$$

Sudanian taxa are included with a weighting factor of 1 in the more humid and with a factor of 0.5 in the more arid phytoregions, because Sudanian plant taxa can penetrate drier regions, for instance, along wadis[91,92]. The combination of grasses (Poaceae) with the wettest group (Guinean) takes into account that they function as the main (biomass) component of savannah vegetation during humid periods (Extended Data Fig. 7c).

Diatom processing and data analysis

Diatom taxonomic and counting analyses were conducted on 0.5-g bulk sediment of 177 samples that were pretreated by standard procedures (1:1 hot mixture of H_2O_2/water, 1:1 hot mixture of HCl/water and repeatedly rinsed in distilled water). Slides were mounted using Naphrax mounting medium (refractive index 1.71)[93]. For each sample, at least 400 diatom valves were identified and counted, except for samples younger than 2.6 kyr BP, which contained few diatoms (<200 valves). A Nikon ECLIPSE 80i and an Olympus BX50 microscope (equipped with differential interference contrast optics at ×1,000 magnification, numerical aperture 1.25) were used for taxonomic identification and counting. Most of the diatoms were identified to their lowest taxonomic level (that is, variety) following the species concept defined by Krammer and Lange-Bertalot[94–96] and using the most recent revised nomenclature[97]. The fossil diatom dataset is based on diatom counts from OUNIK03/04 between 0 and 6,000 calendar years BP (n = 89 samples)[22] and from Co1240 between 6,000 and 10,800 calendar years BP (n = 88 samples; this study). Taxonomic harmonization has been realized on the basis of the references cited above. The data are expressed as relative abundances (%) (Extended Data Fig. 8). Dominant diatom species were identified using multivariate analysis (PCA, CA) based on XLSTAT 2021.4.1 (ref. 98).

A total of 232 diatom species was identified. The diatom taxa were classified according to their preferred habitats based on the ecological classification proposed in ref. 99 and a modern calibration conducted on Ounianga Lakes[100]. Diatom habitats are categorized into planktonic and benthic species. Benthic species include epipelic, epipsammic and epiphytic taxa. Facultative-planktonic taxa are included in the planktonic group. The planktonic to benthic (P/B) ratio, which is known to reveal lake-level fluctuations[101], was calculated for each sample by dividing the number of planktonic by the sum of planktonic, tychoplanktonic and benthic diatoms (Fig. 2b and Extended Data Fig. 8).

A transfer function based on the method of weighted averaging regression[102,103] was developed to infer water conductivity from the diatom data, with a regional dataset including samples from Lake Chad, Lake Fitri and the Ounianga Lakes[100,104]. The dataset includes 119 samples in which 393 species were identified. Statistical treatment of the data enabled to identify, hence remove, statistical 'noise': species with fewer than two occurrences, species with less than 3% maximum relative abundance in the dataset, species with only one occurrence and less than 50% relative abundance and samples with fewer than 200 counted valves. The selected dataset consists of 111 samples and 88 species. This method relies on the calculation of an optimum value for a given hydrochemical parameter—here we focused on the water conductivity—which is the theoretical value for which the species encounters the optimal conditions for its development. The tolerance is a parameter that quantifies the theoretical ability of the species to be maintained if the environmental parameter deviates from the optimum value.

The water conductivity reconstruction, expressed in $\log_{10}$ values and using the tolerance-downweighted weighted averaging, shows the highest performances for both the correlation between diatom-inferred and measured conductivity (R^2 = 0.92) and the root mean square error (RMSE: 0.29 and 0.28 for the classical and inverse deshrinking methods, respectively). The bootstrapping procedure confirms the robust performance of this diatom conductivity transfer function (R^2 = 0.85 and R^2 = 0.84 and RMSEP = 0.43 and RMSEP = 0.43 for the classical and inverse deshrinking methods, respectively), which demonstrates its relevance for application to fossil data. The deshrinking procedure provided regression coefficients of b0 = 0.39 and b1 = 0.83 for the classical method and b0 = −0.22 and b1 = 1.10 for the inverse method.

From the 177 diatom samples analysed from the Lake Yoa record, more than 200 valves were counted in 137 samples. Twenty-two samples after 2.6 kyr BP have counts between 100 and 200 valves from which the diatom-inferred water conductivity should be considered with caution and 17 samples were removed because fewer than 100 valves were counted. Among the 88 species from the modern training set documented in the transfer function, 55 species were observed in the Yoa sequence, accounting for between 40 and 60% of the total relative percentage for 14 samples, between 60 and 80% for 38 samples and more than 80% for 85 samples. After 2.7 kyr BP, *Aulacoseira granulata* was removed from the data, as the valves of this species in the assemblages were attributed to wind dispersion during the corresponding period[22]. Conductivity inferences, calibration statistics and errors were obtained in C2 version 1.3.4 (ref. 105).

Model simulations

Two transient simulations of the Holocene were based on the TraCE simulation using the CCSM3 model and the LOVECLIM model, which were used to evaluate whether external forcings can explain our records (Extended Data Fig. 9). The TraCE simulation included variations in insolation, greenhouse-gas concentrations, ice-sheet extension and altitude from the ICE5-G reconstruction and a crude estimate of associated freshwater release into the North Atlantic. The LOVECLIM model

used similar forcings but included ICE-6G for the ice sheet, an estimate of volcanic forcing, and did not account for freshwater release into the North Atlantic.

The AMOC correction is based on the AMOC reconstruction in ref. 44, which is based on 22 proxy records of sea surface temperature in the North Atlantic, and has a temporal resolution of 50 years and covers the period 10–2 kyr BP. The AMOC reconstruction was calibrated using the Northern Hemisphere reconstruction in ref. 106, transient model simulations and hosting simulations[4,107]. The impact of AMOC variations was quantified after 100 years of 0.3 Sv added to the North Atlantic, leading to freshwater release similar to that estimated during the 8.2 kyr BP event[39]. The variables simulated in the transient run were subsequently corrected using a semi-empirical model described in detail in ref. 107. The effects of the AMOC on precipitation simulated in IPSL-CM6A-LR are similar to those simulated in other models from the North Atlantic Hosing Model Intercomparison Project (NAhosMIP)[20]. However, owing to a lack of availability of the data from other models, we were not able to compute an error bar related to the model used, so the results presented in Extended Data Fig. 9 should be taken as a proof of concept rather than a precise estimate.

For the 8.2 kyr BP water-hosing experiment, the AWI-ESM2.1 model used in this study is a state-of-the-art climate model equipped with water-stable isotope diagnostics[108] developed on the basis of the AWI climate model, version 2 (AWI-ESM2). The model consists of an ice-ocean component, FESOM2 (refs. 109–111), whose structure is based on a finite-volume approach[109,111], and the atmosphere general circulation model ECHAM6 (ref. 112), which incorporates diabatic processes with large-scale circulation of the atmosphere and contains the dynamic vegetation model JSBACH[113–115]. Three water-stable isotope tracers are further added to all relevant processes in the water cycle[108]. This model has already been applied in several studies covering a wide range of climate conditions involving the present day[111], the latest Holocene[116], the Last Glacial Maximum[117], the Last Interglacial[118] and the Miocene[119].

With AWI-ESM2.1-wiso, we performed equilibrium simulations for the early Holocene, in which we fixed the boundary conditions at 8.2 kyr BP (Extended Data Fig. 10b), following the simulations in ref. 120. The greenhouse-gas concentrations were taken from ice-core records[121]. The topography and ice-sheet properties were derived from the GLAC1D reconstruction. The atmosphere model resolution is T63 (about 1.9°) in the horizontal domain with 47 vertical levels. The resolution for the ocean reaches 20 km in polar and coastal areas and 35–50 km across the equatorial belt. We integrated the early Holocene experiment for 1,000 model years, with no obvious trends observed for the final 100 model years. Then, to reproduce the 8.2 kyr BP cold event, we extended the simulation by adding 0.15 Sv of freshwater over the Labrador Sea for another 100 model years (Fig. 4 and Extended Data Fig. 10d).

Data availability

All data that support this study are available from Zenodo with reference to the paper (including all information and references to the paper) at https://doi.org/10.5281/zenodo.13912623 (ref. 26). The maps in Fig. 1 were made with the software ArcMap 10.6 (Esri Inc.) using background maps (Fig. 1b: maps data: Google, 2022, Landsat/Copernicus; Fig. 1c: maps data: Google, 2024, Maxar Technologies). The water drainage map in Extended Data Fig. 1a and the swath profile in Extended Data Fig. 1b are based on the Advanced Spaceborne Thermal Emission and Reflection Radiometer (ASTER) Global Digital Elevation Model (GDEM) and made using ArcMap 10.6 (Esri Inc.).

48. Mahamoud, A. H. Geologie und Hydrogeologie des Erdis-Beckens, NE-Tschad. In *Berliner Geowissenschaftliche Abhandlungen A/76* (Dietrich Reimer Verlag, 1986).
49. Wolff, J. P. Carte géologique de la République du Tchad au 1/1.500.000e (BRGM Paris, 1964).
50. Elsheikh, A. A., Abdelsalam, M. G. & Mickus, K. Geology and geophysics of the West Nubian Paleolake and the Northern Darfur Megalake (WNPL–NDML): implication for groundwater resources in Darfur, northwestern Sudan. *J. Afr. Earth Sci.* **61**, 82–93 (2011).
51. Gossel, W., Ebraheem, A. M. & Wycisk, P. A very large scale GIS-based groundwater flow model for the Nubian sandstone aquifer in Eastern Sahara (Egypt, northern Sudan and eastern Libya). *Hydrogeol. J.* **12**, 698–713 (2004).
52. Poulin, C. *Bilans hydrologiques et étude de la recharge de trois systèmes lac-aquifère du Bassin du Lac Tchad par une approche géochimique multi traceurs ($\delta^{18}O$, $\delta^{2}H$, ^{36}Cl, ^{14}C).* Thèse de Doctorat, Aix-Marseille Université (2019).
53. Nicholson, S. E. The nature of rainfall variability over Africa on time scales of decades to millenia. *Glob. Planet. Change* **26**, 137–158 (2000).
54. Ministère de l'Eau et de l'Assainissement de la République du Tchad. Synthèse hydrogéologique du nord et de l'est du Tchad (2016).
55. Capot-Rey, R. Borkou et Ounianga, Étude de géographie régionale. Université d'Alger, Institut de Recherches Sahariennes, Mémoire 5 (1961).
56. Washington, R. et al. Links between topography, wind, deflation, lakes and dust: the case of the Bodélé Depression, Chad. *Geophys. Res. Lett.* **33**, L09401 (2006).
57. Lézine, A.-M., Zheng, W., Braconnot, P. & Krinner, G. Late Holocene plant and climate evolution at Lake Yoa, northern Chad: pollen data and climate simulations. *Clim. Past* **7**, 1351–1362 (2011).
58. Remadji, R. et al. Modern diatom calibration data from Saharan lakes for inferring hydrochemistry. *J. Paleolimnol.* **69**, 231–248 (2023).
59. van de Meeren, T. et al. in *Le Tchad des Lacs. Les Zones Humides Sahéliennes au Défi du Changement Global* (eds Raimond, C., Sylvestre, F., Zakinet, D. & Abderamane, M.) 127–138 (IRD, 2019).
60. Vandenberghe, J. Grain size of fine-grained windblown sediment: a powerful proxy for process identification. *Earth Sci. Rev.* **121**, 18–30 (2013).
61. Appleby, P. G. in *Tracking Environmental Change Using Lake Sediments: Basin Analysis, Coring, and Chronological Techniques* (eds Last, W. M. & Smol, J. P.) 171–203 (Kluwer, 2001).
62. Rethemeyer, J. et al. Status report on sample preparation facilities for ^{14}C analysis at the new CologneAMS center. *Nucl. Instrum. Methods Phys. Res. B* **294**, 168–172 (2013).
63. Uchikawa, J., Popp, B. N., Schoonmaker, J. E. & Xu, L. Direct application of compound-specific radiocarbon analysis of leaf waxes to establish lacustrine sediment chronology. *J. Paleolimnol.* **39**, 43–60 (2008).
64. Bronk Ramsey, C. Bayesian analysis of radiocarbon dates. *Radiocarbon* **51**, 337–360 (2009).
65. Reimer, P. et al. The IntCal20 Northern Hemisphere radiocarbon age calibration curve (0–55 cal kBP). *Radiocarbon* **62**, 725–757 (2020).
66. Philippsen, B. The freshwater reservoir effect in radiocarbon dating. *Herit. Sci.* **1**, 24 (2013).
67. Blott, S. J. & Pye, K. GRADISTAT: a grain size distribution and statistics package for the analysis of unconsolidated sediments. *Earth Surf. Process. Landf.* **26**, 1237–1248 (2001).
68. Folk, R. L. & Ward, W. C. Brazos River bar [Texas]; a study in the significance of grain size parameters. *J. Sediment. Res.* **27**, 3–26 (1957).
69. Croudace, I. W., Rindby, A. & Rothwell, R. G. ITRAX: description and evaluation of a new multi-function X-ray core scanner. *Geol. Soc. Lond. Spec. Publ.* **267**, 51–63 (2006).
70. Eisele, G., Haas, K. & Liner, S. in *Über Probleme der holozänen Vegetationsgeschichte Osttibets. Göttinger Geographische Abhandlungen* (ed. Frenzel, B.) 165–166 (Institute of Geography of the University of Göttingen, 1994).
71. Nakagawa, T. et al. Dense-media separation as a more efficient pollen extraction method for use with organic sediment/deposit samples: comparison with the conventional method. *Boreas* **27**, 15–24 (1998).
72. Moore, P. D., Webb, J. A. & Collinson, M. E. *Pollen Analysis* 2nd edn (Blackwell, 1991).
73. Bonnefille, R. & Riollet, G. *Pollens des Savanes d'Afrique Orientale* (CNRS Éditions, 1980).
74. El Ghazali, G. A study on the pollen flora of Sudan. *Rev. Palaeobot. Palynol.* **76**, 99–345 (1993).
75. El-Ghazali, G. *Pollen Flora of Qatar* (Scientific and Applied Research Center, Univ. Qatar, 1991).
76. Gosling, W. D., Miller, C. S. & Livingstone, D. A. Atlas of the tropical West African pollen flora. *Rev. Palaeobot. Palynol.* **199**, 1–135 (2013).
77. Maley, J. Contributions à l'étude du bassin tchadien. Atlas de pollens du Tchad. *Bull. Jard. Bot. Natl Belg.* **40**, 29–48 (1970).
78. Schüler, L. & Hemp, A. Atlas of pollen and spores and their parent taxa of Mt Kilimanjaro and tropical East Africa. *Quat. Int.* **425**, 301–386 (2016).
79. Sowunmi, M. Pollen grains of Nigerian plants. *Grana* **13**, 145–186 (1973).
80. Sowunmi, M. Pollen of Nigerian plants. *Grana* **34**, 120–141 (1995).
81. Lézine, A.-M., Ivory, S. J., Gosling, W. D. & Scott, L. in *Quaternary Vegetation Dynamics. The African Pollen Database* (eds Gosling, W., Lézine, A. M. & Scott, L.) 5–13 (CRC, 2022).
82. Martin, A. C. & Harvey, W. J. The Global Pollen Project: a new tool for pollen identification and the dissemination of physical reference collections. *Methods Ecol. Evol.* **8**, 892–897 (2017).
83. MUPA members. Montpellier University Pollen Atlas. OSU OREME Collection (2018).
84. APSA Members. Australasian Pollen and Spore Atlas V1.0. Australian National University. http://apsa.anu.edu.au/ (2007).
85. PalDat – Palynological database. https://www.paldat.org/.
86. PCU Pollen Database. https://science.uct.ac.za/plant-conservation/resources-databases/pcu-pollen-database.
87. Djamali, M. & Cilleros, K. Statistically significant minimum pollen count in Quaternary pollen analysis; the case of pollen-rich lake sediments. *Rev. Palaeobot. Palynol.* **275**, 104156 (2020).
88. White, F. *The Vegetation of Africa; A Descriptive Memoir to Accompany the UNESCO/AETFAT/UNSO Vegetation Map of Africa* (UNESCO, 1983).
89. Hély, C. et al. Holocene changes in African vegetation: trade-off between climate and water availability. *Clim. Past* **10**, 681–686 (2014).
90. Vincens, H. et al. African pollen database inventory of tree and shrub pollen types. *Rev. Palaeobot. Palynol.* **145**, 135–141 (2007).
91. Wickens, G. E. A study of *Acacia albida*. *Kew Bull.* **23**, 181–202 (1969).
92. Walter, H. & Breckle, S. *Ökologie der Erde. Band 1. Ökologische Grundlagen in globaler Sicht. 2. Auflage* (Gustav Fischer Verlag, 1991).
93. Battarbee, R. W., Jones, V. J., Flower, R. J., Cameron, N. G. & Bennion, H. in *Tracking Environmental Change Using Lake Sediments* (eds Smol J. P., Birks H. J. B. & Last, W. M.) 155–202 (Kluwer, 2001).

94. Krammer, K. & Lange-Bertalot, H. *Süsswasserflora von Mitteleuropa. Bacillariophyceae. Teil 1: Naviculaceae* (Gustav Fischer Verlag, 1986).
95. Krammer, K. & Lange-Bertalot, H. *Süsswasserflora von Mitteleuropa. Bacillariophyceae. Teil 2: Bacillariaceae, Epithemiaceae, Surirellaceae* (Gustav Fischer Verlag, 1988).
96. Krammer, K. & Lange-Bertalot, H. *Süsswasserflora von Mitteleuropa. Bacillariophyceae. Teil 3: Centrales, Fragilariaceae, Eunotiaceae* (Gustav Fischer Verlag, 1991).
97. Guiry M. D. & Guiry G. M. AlgaeBase. World-wide electronic publication, University of Galway. https://www.algaebase.org (2022).
98. Addinsoft. XLSTAT statistical and data analysis solution. https://www.xlstat.com (2022).
99. Gasse, F. East *African Diatoms. Taxonomy, Ecological Distribution. Bibliotheca Diatomologica, Band 11* (J. Cramer, 1986).
100. Rirongarti, R. et al. Modern diatom calibration data from Saharan lakes for inferring hydrochemistry. *J. Paleolimnol*. **69**, 231–248 (2023).
101. Wolin, J. A. & Stone, J. R. in *The Diatoms: Applications for the Environmental and Earth Sciences* 2nd edn (eds Smol J. P. & Stoermer E. F.) (Cambridge Univ. Press, 2010).
102. Ter Braak, C. J. F. & Looman, C. W. N. Weighted averaging, logistic regression and the Gaussian response model. *Vegetation* **65**, 3–11 (1986).
103. Birks, H. J. B., Line, J. M., Juggins, S., Stevenson, A. C. & Ter Braak, C. J. F. Diatoms and pH reconstruction. *Philos. Trans. R. Soc. Lond. B* **327**, 263–278 (1990).
104. Rirongarti R. *Etude des Diatomées Actuelles des Lacs du Tchad: Taxonomie, Diversité et Calibration*. Thèse de Doctorat, Université d'Aix-Marseille (2019).
105. Juggins, S. C*2 User Guide. Software for Ecological and Palaeoecological Data Analysis and Visualisation* (Univ. Newcastle, 2003).
106. Kaufman, D. et al. A global database of Holocene paleotemperature records. *Sci. Data* **7**, 115 (2020).
107. Jomelli, V. et al. In-phase millennial-scale glacier changes in the tropics and North Atlantic regions during the Holocene. *Nat. Commun.* **13**, 1419 (2022).
108. Shi, X. et al. Simulated stable water isotopes during the mid-Holocene and pre-industrial periods using AWI-ESM-2.1-wiso. *Geosci. Model. Dev.* **16**, 5153–5178 (2023).
109. Danilov, S., Sidorenko, D., Wang, Q. & Jung, T. The finite-volume sea ice–ocean model (FESOM2). *Geosci. Model. Dev.* **10**, 765–789 (2017).
110. Scholz, P. et al. Assessment of the Finite-volumE Sea ice-Ocean Model (FESOM2.0) – part 1: description of selected key model elements and comparison to its predecessor version. *Geosci. Model. Dev.* **12**, 4875–4899 (2019).
111. Sidorenko, D. et al. Evaluation of FESOM2.0 coupled to ECHAM6.3: preindustrial and HighResMIP simulations. *J. Adv. Model. Earth Syst.* **11**, 3794–3815 (2019).
112. Stevens, B. et al. Atmospheric component of the MPI-M Earth system model: ECHAM6. *J. Adv. Model. Earth Syst.* **5**, 146–172 (2013).
113. Giorgetta, M. A. et al. Climate and carbon cycle changes from 1850 to 2100 in MPI-ESM simulations for the Coupled Model Intercomparison Project phase 5. *J. Adv. Model. Earth Syst.* **5**, 572–597 (2013).
114. Raddatz, T. J. et al. Will the tropical land biosphere dominate the climate–carbon cycle feedback during the twenty-first century? *Clim. Dyn.* **29**, 565–574 (2007).
115. Reick, C. H., Raddatz, T., Brovkin, V. & Gayler, V. Representation of natural and anthropogenic land cover change in MPI-ESM. *J. Adv. Model. Earth Syst.* **5**, 459–482 (2013).
116. Vorrath, M. E. et al. Sea ice dynamics in the Bransfield Strait, Antarctic Peninsula, during the past 240 years: a multi-proxy intercomparison study. *Clim. Past* **16**, 2459–2483 (2020).
117. Kageyama, M. et al. The PMIP4 Last Glacial Maximum experiments: preliminary results and comparison with the PMIP3 simulations. *Clim. Past* **17**, 1065–1089 (2021).
118. Otto-Bliesner, B. L. et al. Large-scale features of last interglacial climate: results from evaluating the *lig*127k simulations for the Coupled Model Intercomparison Project (CMIP6)–Paleoclimate Modeling Intercomparison Project (PMIP4). *Clim. Past* **17**, 63–94 (2021).
119. Hossain, A. et al. The impact of different atmospheric CO_2 concentrations on large scale Miocene temperature signatures. *Paleoceanogr. Paleoclimatol.* **38**, e2022PA004438 (2023).
120. Shi, X., Lohmann, G., Sidorenko, D. & Yang, H. Early-Holocene simulations using different forcings and resolutions in AWI-ESM. *Holocene* **30**, 996–1015 (2020).
121. Köhler, P. et al. A 156 kyr smoothed history of the atmospheric greenhouse gases CO_2, CH_4, and N_2O and their radiative forcing. *Earth Syst. Sci. Data* **9**, 363–387 (2017).

Acknowledgements This study was financed mainly by the German Research Foundation (DFG, grant number 57444011) as part of the Collaborative Research Center CRC 806 – 'Our Way to Europe'. The contribution of M.D. was supported by the DFG Priority Programme SPP 2143 'Entangled Africa' (project number 404354295) and that of A.D. by PalMod (grant no. 01LP1920A), financed by the German Federal Ministry of Education and Research (BMBF), Research for Sustainability initiative (FONA). Support to X.S. was provided by the Southern Marine Science and Engineering Guangdong Laboratory (Zhuhai) (grant no. SML2023SP204), the Guangdong Basic and Applied Basic Research Foundation (grant no. 2025A1515012165) and the Ocean Negative Carbon Emissions (ONCE) programme. This study was also supported by the French National Research Institute for Sustainable Development (IRD) and the French Embassy in Chad within the framework of the 'Grands Ecosystèmes Lacustres Tchadiens (GELT)' FSP 2013-18 project. We thank the Chadian Institute for Research and Development (CNAR) for its support and the permit for the study (permit no. 025/CNAR/10). S. Oehm, D. Furkert and C. Lederer (University of Cologne) and A. M. Anur (Centre National De Recherche Pour le Développement (CNRD) N'Djamena) are acknowledged for their help in the fieldwork on Lake Yoa, and N. Mantke (University of Cologne) and R. Kreutz (Marum Bremen) for their analytical support. We thank A. Cohen and P. Valdes for their fruitful and constructive comments that have improved the manuscript substantially.

Author contributions F.S., M.M. and V.W. designed the paper and prepared the original manuscript. S.K. initiated and has led the field research at the Lakes of Ounianga since 1999. M.M., S.K., B.M. and J. Karls realized the coring campaign. M.M., V.W. and J. Karls provided the core lithology, chronology, grain size, geochemical and XRF data. A.N.Y. contributed to the geological and palaeoenvironmental background of the Ounianga area and the central Sahara. F.S. and C.C. provided the diatom data and fossil taxonomy assemblages. J.-C.M. and C.P. contributed to the diatom preparation samples and taxonomic determination. F.C. and R.R. designed the diatom-based transfer function. M.D. provided the palynological analysis. A.J. and E.S. provided compound-specific isotope data for the plant waxes. B.R.-P. provided map generation and geo-hydrological modelling. J. Karls, J. Kuper and J.R. contributed to the development of the age–depth model of core Co1240 and B.W. and F.V. supported the interpretation of the sediment proxy data. D.S. ran the AMOC simulations. A.D., X.S., M.C. and M.W. ran and analysed the modelling experiments. All authors contributed to the discussion of the results and commented on the manuscript.

Competing interests The authors declare no competing interests.

Additional information

Supplementary information The online version contains supplementary material available at https://doi.org/10.1038/s41586-026-10336-7.

Correspondence and requests for materials should be addressed to Florence Sylvestre.

Peer review information *Nature* thanks Andrew Cohen, Paul Valdes and the other, anonymous, reviewer(s) for their contribution to the peer review of this work. Peer reviewer reports are available.

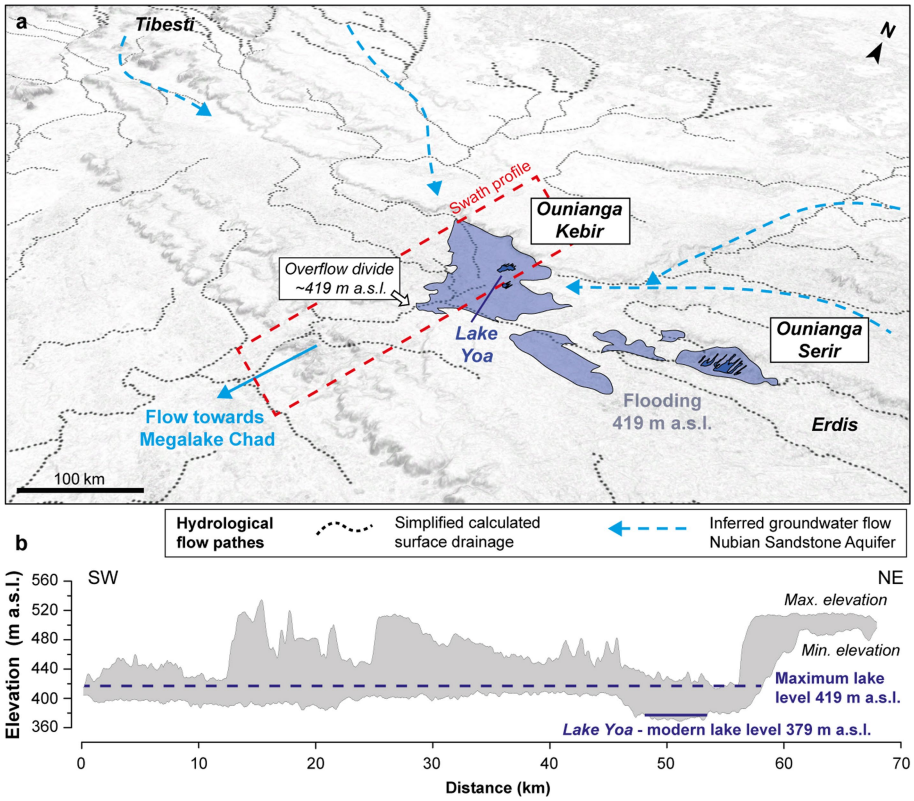

Extended Data Fig. 1 | Geomorphological and hydrometric context of the Ounianga Lakes district. a, Water drainage to Ounianga Serir and Ounianga Kebir based on Advanced Spaceborne Thermal Emission and Reflection Radiometer (ASTER) Global Digital Elevation Model (GDEM) data using ArcMap 10.6 with the main Lake Yoa (dark-blue shading) and the potential sizes of lakes formed by flooding up to 419 m above sea level (a.s.l.) (light-blue shading), as suggested by exposed diatomites and a potential overflow divide at 419 m according to ref. 21. **b**, Elevation ranges (m a.s.l.) from a southwest–northeast swath profile (based on ASTER GDEM; for location, see dashed red frame in **a**), superimposed by the current water level of Lake Yoa (continuous blue line) and its maximum level during the AHP (dashed blue line).

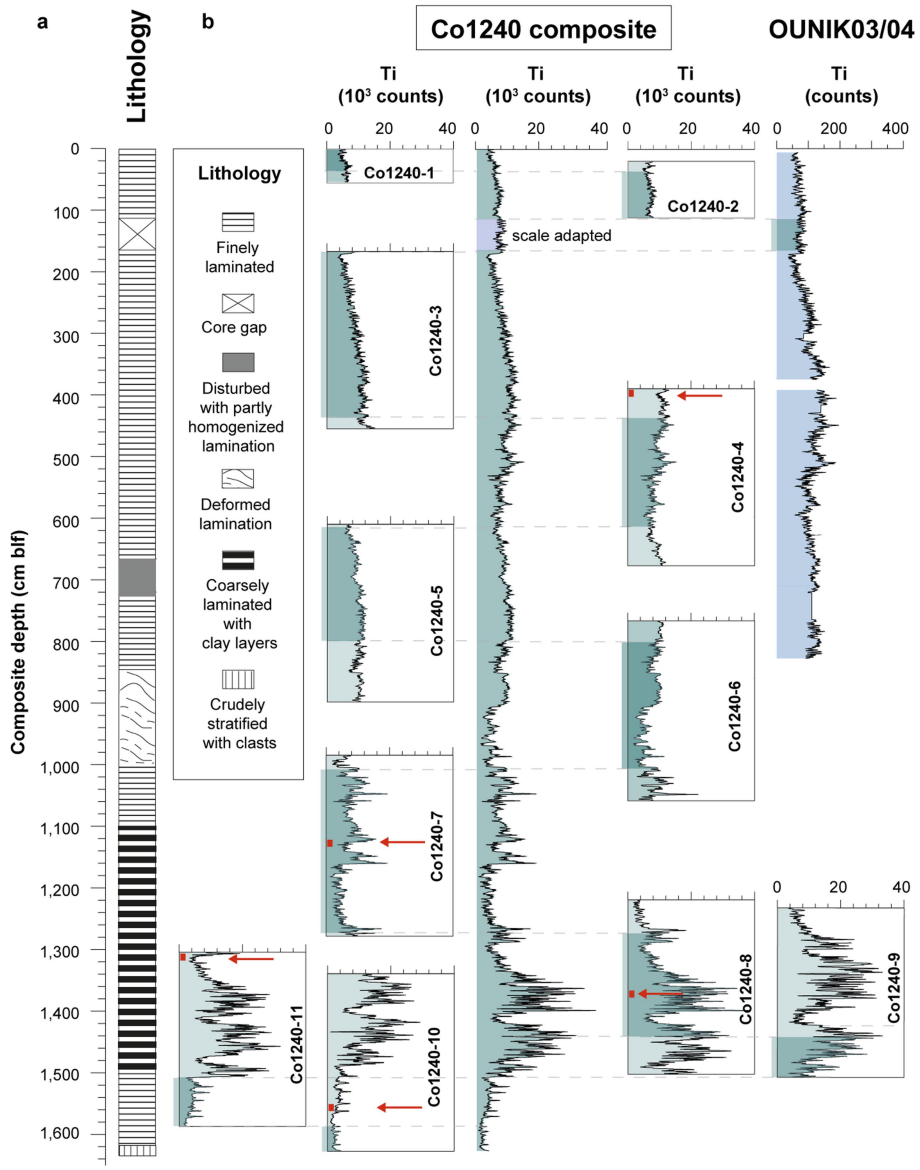

Extended Data Fig. 2 | Construction of the Co1240 composite core. a, Core Co1240 lithology with a core gap and bedding types. **b**, The composite core (central column) is based on the correlation of lithological changes and Ti XRF counts of the cores Co1240 and OUNIK03/04. Core segments building the composite are highlighted with darker shading and dashed lines. The red arrows and rectangles mark the positions of the thin sections shown in Extended Data Fig. 5.

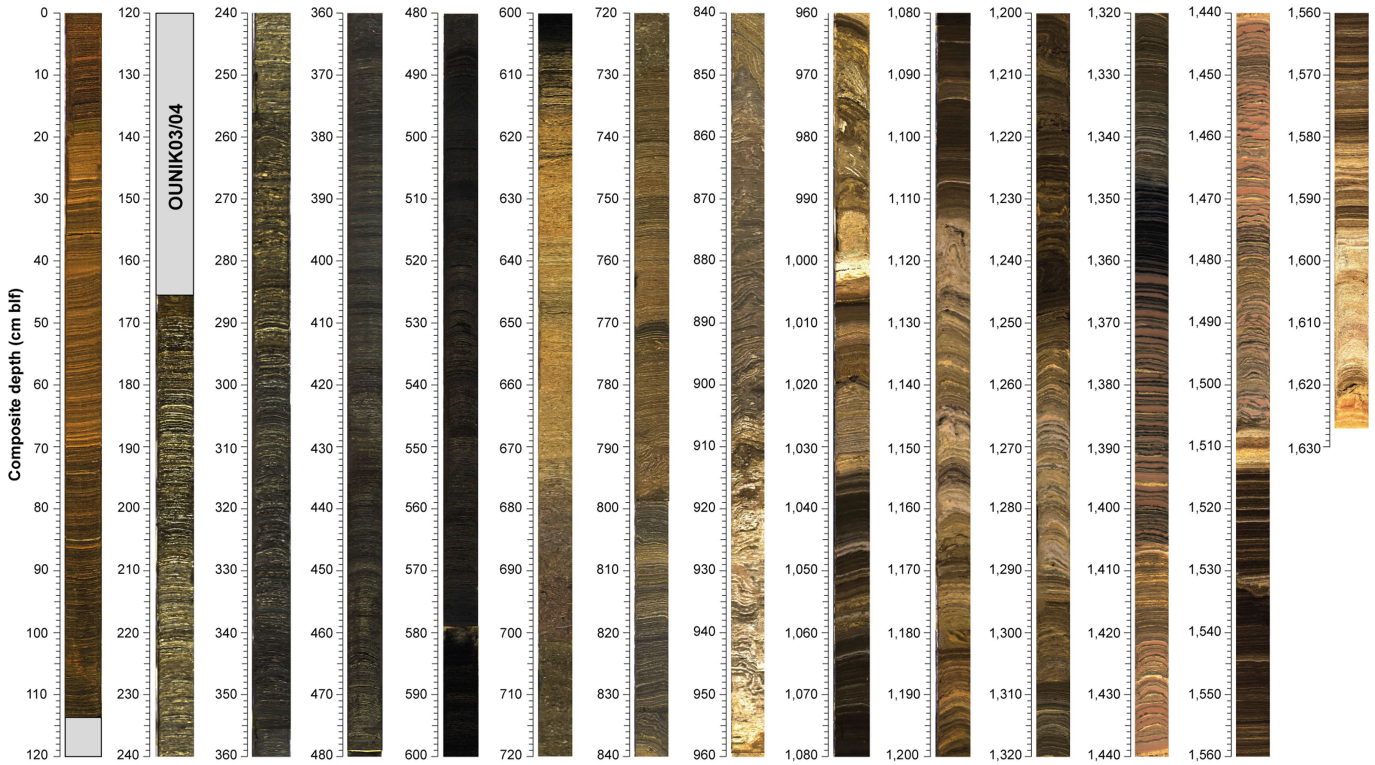

Extended Data Fig. 3 | Linescan images of the composite core Co1240. For classified bedding types, see Extended Data Fig. 2.

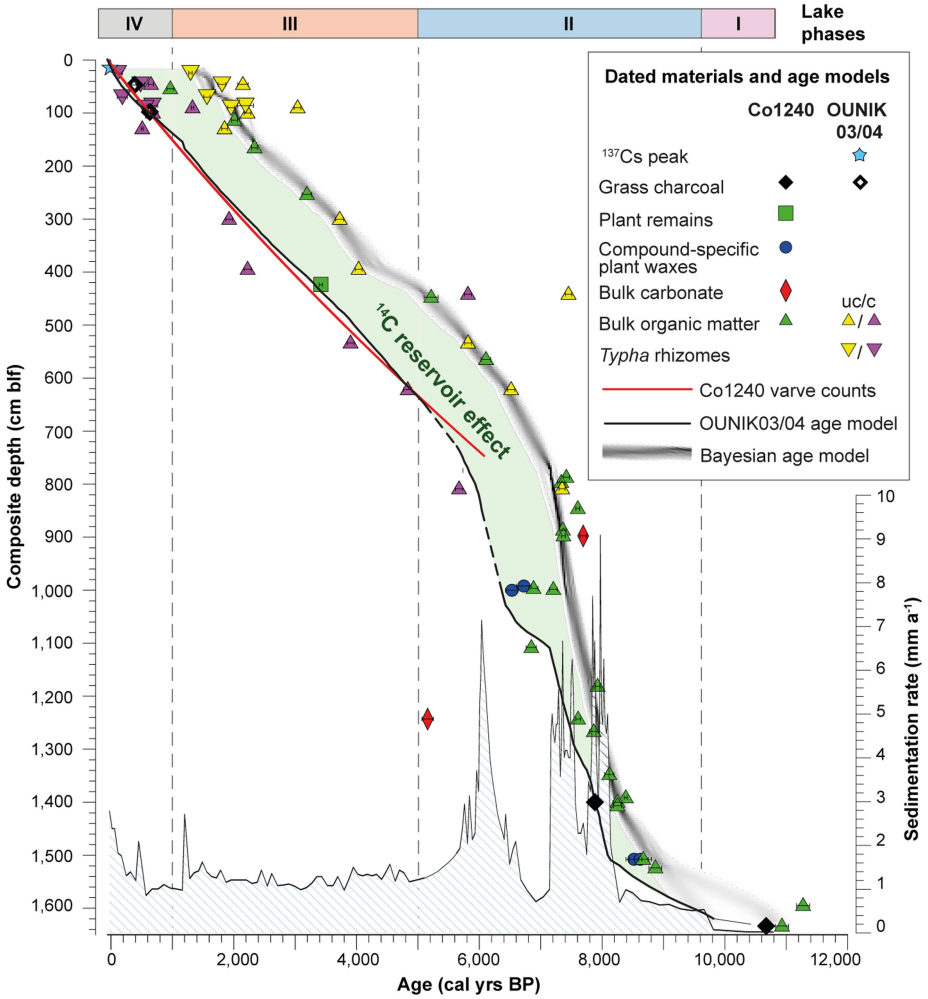

Extended Data Fig. 4 | Chronology of the composite core Co1240. The chronology of Co1240 is based on varve counting (black line, hatched where extrapolated), supported by the AD 1963 ^{137}Cs peak and ^{14}C ages of grass charcoal and plant remains[26] (compare with Extended Data Fig. 6). The resultant sedimentation rates are indicated by the striped pattern. Also shown are the chronology of core OUNIK03/04 (ref. 22) (red line), the four lake phases (at the top of the figure and dashed lines), ^{14}C ages of bulk carbonate and compound-specific plant waxes and uncorrected (uc) and reservoir-corrected (c) ^{14}C ages of bulk organic matter and *Typha* rhizomes. The uncorrected ^{14}C ages of organic matter and *Typha* rhizomes were used for the Bayesian age–depth model (grey shading), whose differences to the varve chronology (green shading) reflect the variable reservoir effects associated with the radiocarbon ages of these components.

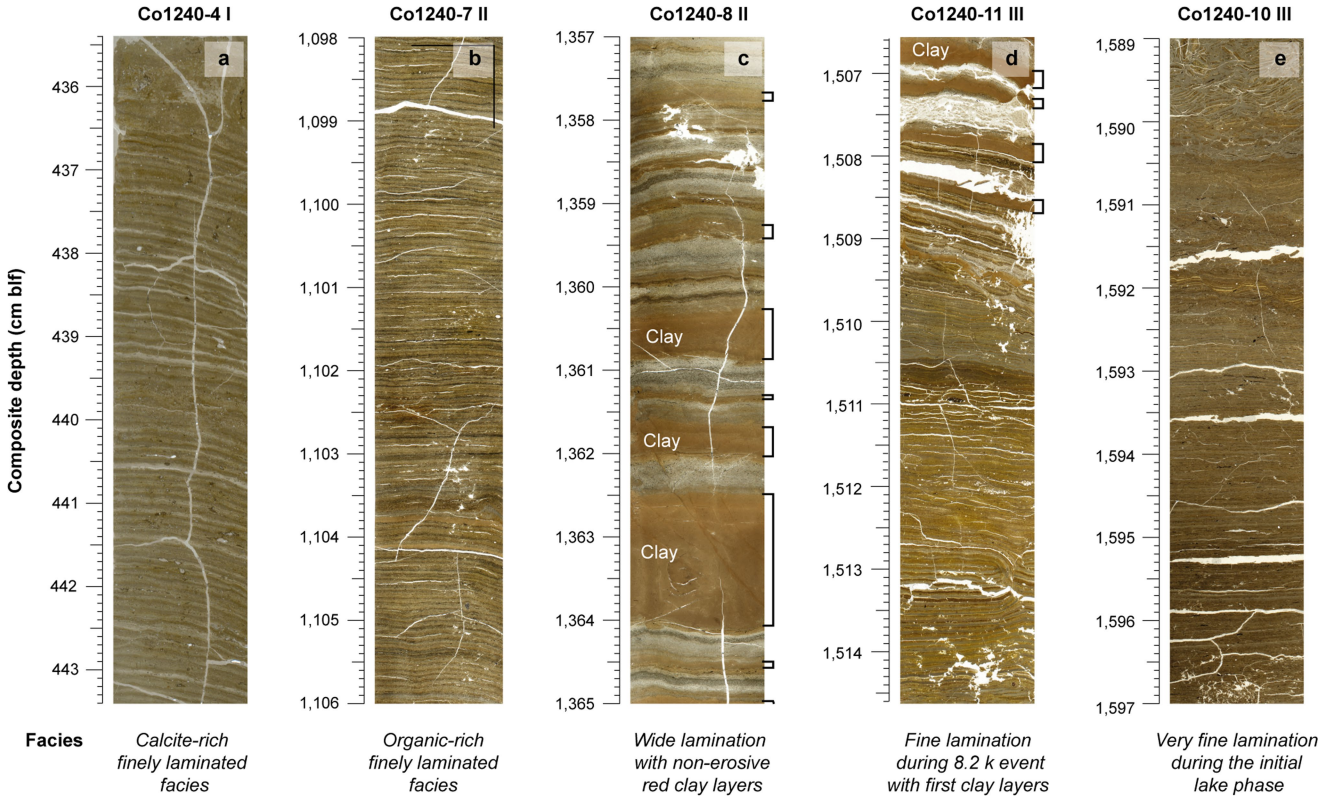

Extended Data Fig. 5 | Exemplary thin sections from core Co1240. For positions of thin sections, see red arrows and rectangles in Extended Data Fig. 2. **a**, Calcite-rich finely laminated sediment in the upper core part corresponding to the lower laminated facies in core OUNIK03/04 (ref. 23) that has proved to represent annual layers (varves). **b**, Finely laminated sediment similar to **a** in larger sediment depth, below the two disturbed intervals in core Co1240. **c**, Coarsely laminated sediment with intercalated non-erosive, reddish-brown clay layers (indicated by black rectangles and partly labelled). **d**, Finely laminated sediment deposited during the 8.2 kyr event and first clay layers above (indicated by black rectangles). **e**, Particularly finely laminated sediment deposited during the initial stage of Lake Yoa.

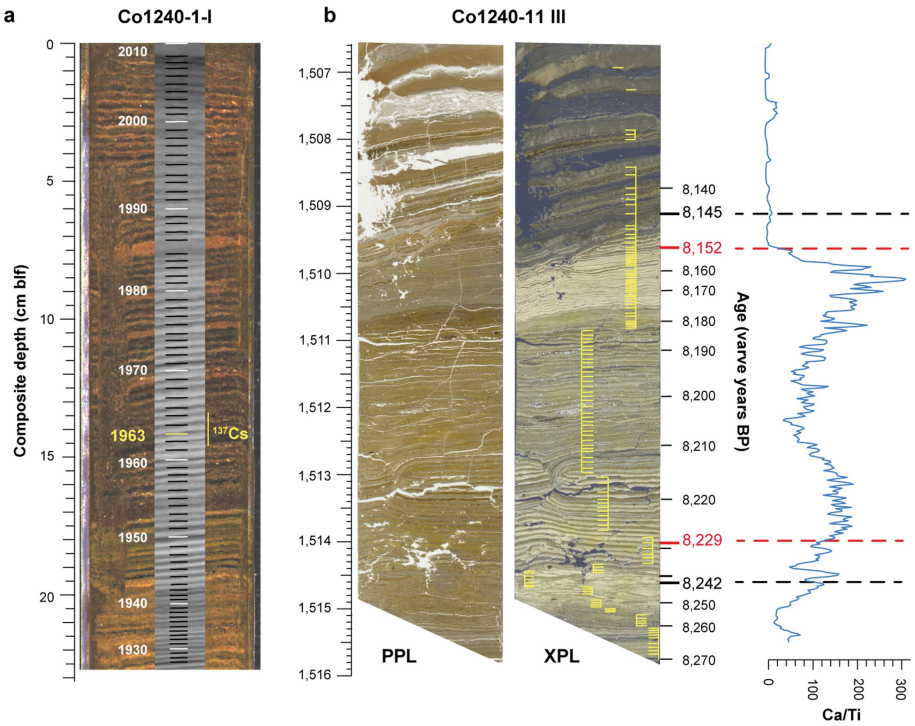

Extended Data Fig. 6 | Annual layering in core Co1240. a, High-resolution linescan colour image of the upper 22.7 cm in the gravity core Co1240-1 that forms the uppermost part of the composite core (Extended Data Fig. 2). Superimposed is the greyscale image of X-radiographs, with the layer counting indicated by black and white lines. Also shown is the depth of the ^{137}Cs peak ascribed to AD 1963, which was measured in core OUNIK03/04 (Fig. 1) and transferred to Co1240-1 based on the correlation of comparable lamination patterns in both cores (Methods). The perfect match of the ^{137}Cs peak with the layer counts confirms their annual formation as varves. **b**, Thin section from 1,506.5–1,516.0 cm, bracketing the 8.2 kyr BP drought event. The thin section is shown in plane (PPL) and cross-polarized light (XPL), with the varve counts superimposed (yellow lines) and the sediment depths and varve ages before present indicated. The Ca/Ti ratio, measured along the centre of the thin section in 200-µm resolution, illustrates the amounts of calcite precipitation relative to clastic sedimentation.

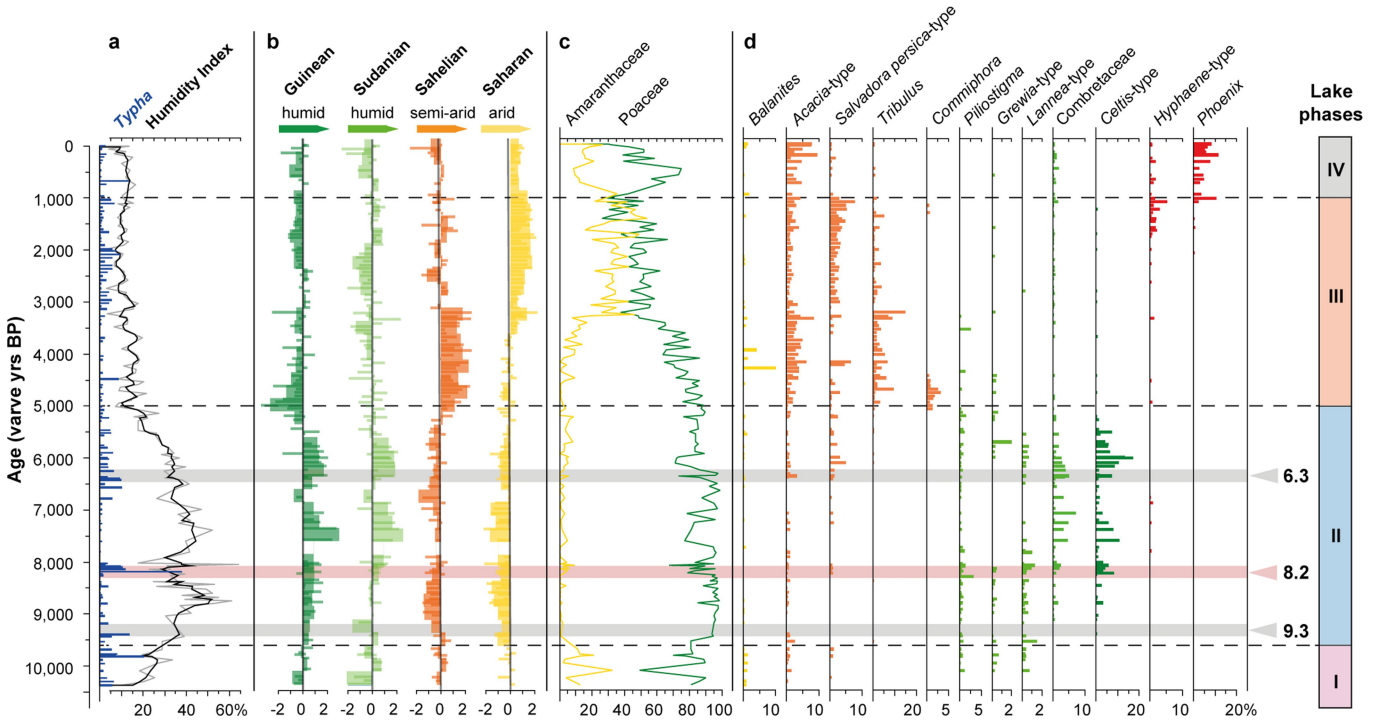

Extended Data Fig. 7 | The Lake Yoa pollen record. The record is based on pollen counts from cores OUNIK03/04 (<5.2 kyr BP)[22] and Co1240 (>5.2 kyr BP) (Fig. 1). **a**, Pollen-derived HI and *Typha* as an indicator of extended littoral vegetation. **b**, *z*-scores of the summed proportions of Guinean, Sudanian, Sahelian and Saharan taxa, calculated from squared-root-transformed and centre-log-ratio-transformed values. Phytochoria groups are colour-coded according to moisture: positive values (on the right) of the Guinean (dark green) and Sudanian (light green) curves show the spread of these taxa indicative of humid conditions; values to the left (negative) their decrease, indicating reduced plant-available moisture; positive values of the Sahelian taxa (orange) indicate semi-arid conditions and shifts of the Saharan taxa (yellow) to positive values indicate the establishment of today's desert vegetation under arid conditions. The small bars show the samples; the larger, semi-transparent bars correspond to 250 years average. **c**, Percentage variations of the main phytomass producers, that is, grasses (Poaceae) and Amaranthaceae (sum of *Cornulaca*-type and *Amaranthus*-type), which mainly reflect savannah and desert vegetation, respectively. **d**, Percentages of selected pollen types showing the main vegetation changes. The colours of the pollen types correspond to their respective phytogeographical affinity. The column on the right and the dashed lines indicate the four phases of long-term hydrological changes, the grey and red horizontal bars the superimposed short-term droughts during phase II.

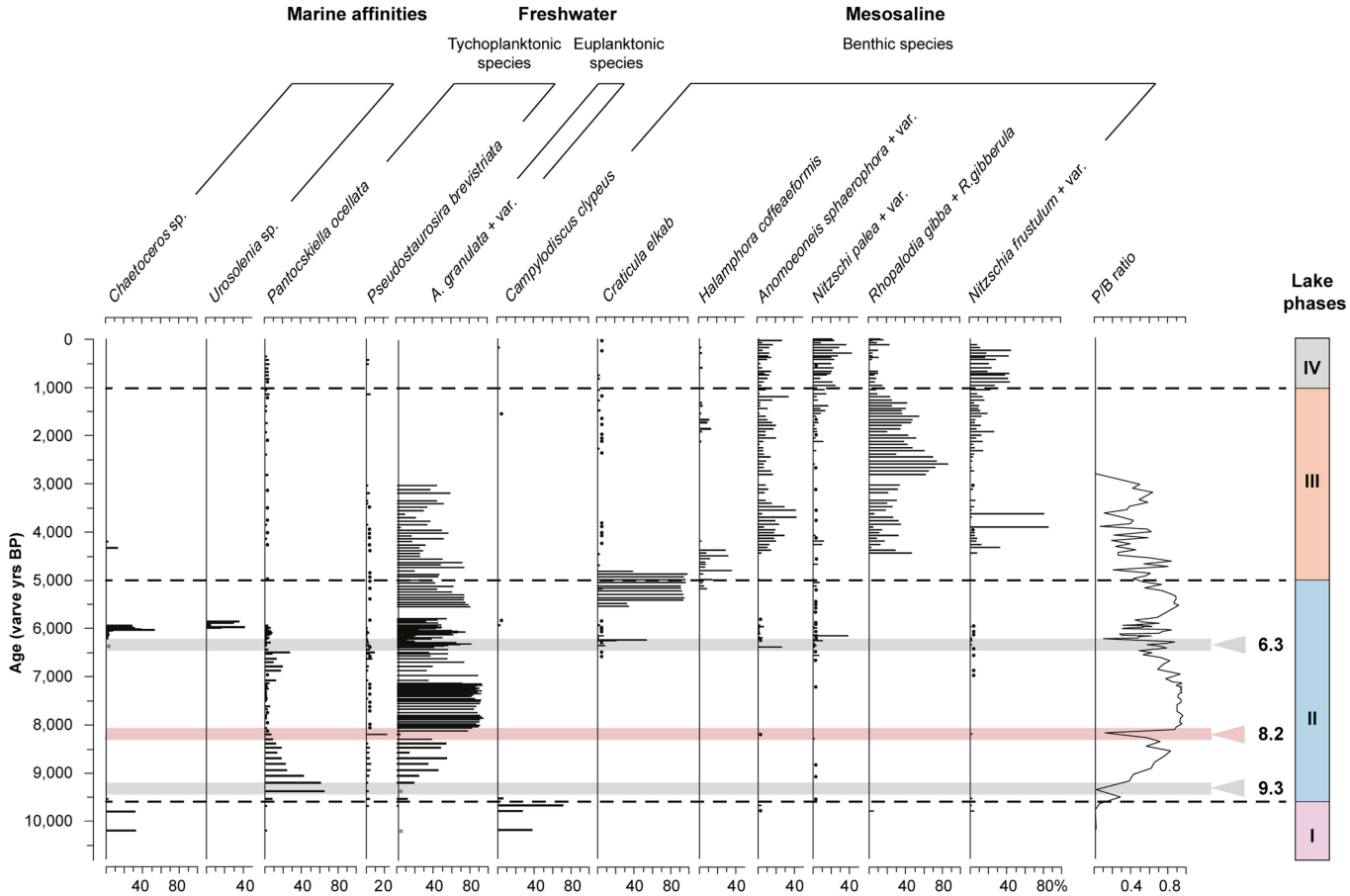

Extended Data Fig. 8 | The Lake Yoa diatom record. The record is based on diatom counts from cores OUNIK03/04 (<6.0 kyr BP)[22] and Co1240 (>6.0 kyr BP) (Fig. 1). Taxa are presented according to their preferred habitats and the resultant P/B diatom ratio, as shown in Fig. 2b. The column on the right side and the dashed lines indicate the four phases of long-term hydrological changes, the grey and red horizontal bars the superimposed short-term droughts during phase II.

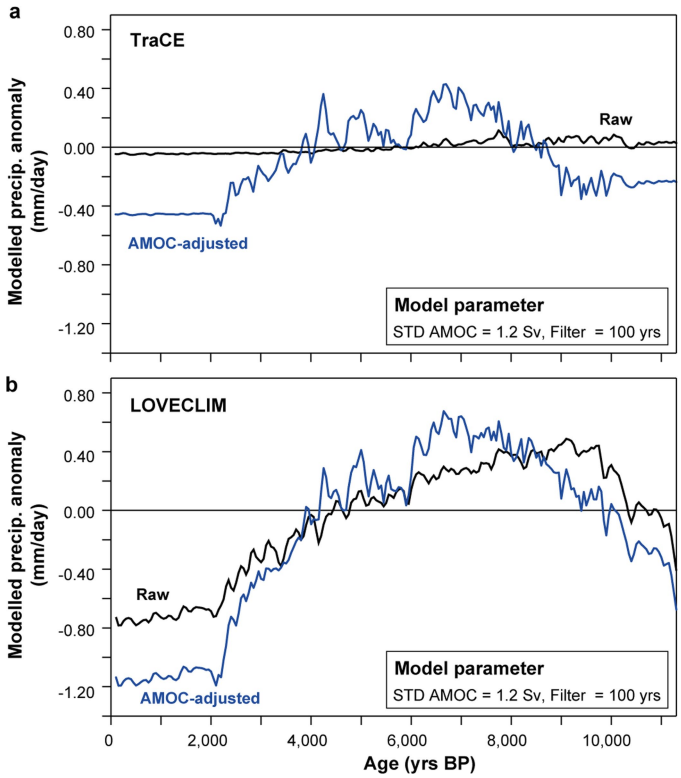

Extended Data Fig. 9 | Transient Holocene precipitation simulations for the Lake Yoa area. a, Results of the TraCE model. **b**, Results of the LOVECLIM model. Black and blue lines indicate simulations without and with AMOC correction, respectively.

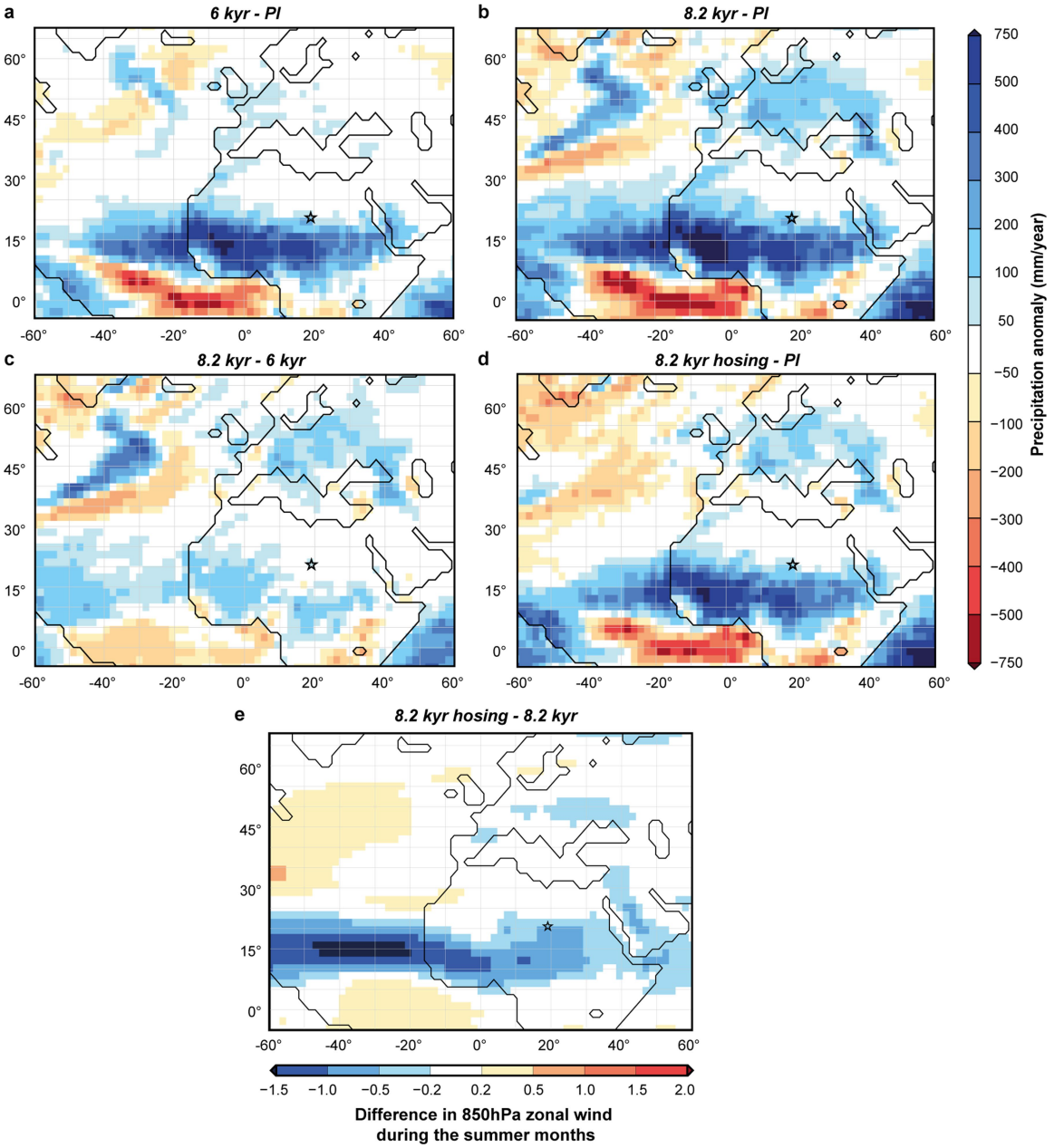

Extended Data Fig. 10 | Simulated in monsoon changes for the 8.2 kyr BP event. a–**d**, Annual mean precipitation anomalies simulated by AWI-ESM between 6 kyr BP and the preindustrial period (PI) (**a**), 8.2 kyr BP without hosing and PI (**b**), 8.2 kyr BP without hosing and 6 kyr BP (**c**) and 8.2 kyr BP with hosing and PI (**d**). **e**, Difference in 850 hPa zonal wind during the summer months (June, July, August, September) between 8.2 kyr BP with hosing and 8.2 kyr BP without hosing. The location of Lake Yoa is marked by stars.